

Topological Signatures of the Optical Bound on Maximal Berry Curvature: Application to Two-Dimensional Time-Reversal Symmetric Insulators

Pok Man Chiu*

Graduate Institute of Applied Physics, National Chengchi University, Taipei City 11605, Taiwan and
Department of Physics, National Tsing Hua University, Hsinchu 30013, Taiwan

(Dated: January 12, 2026)

Unlike broken time-reversal symmetric (TRS) systems with a defined Chern number, directly measuring the bulk Z_2 invariant and Berry curvature (if nonzero) in topological insulators and their higher-order topological families remains an unsolved problem. Here, based on the refined trace-determinant inequality (TDI) involving the trace and determinant of the quantum metric and maximal Berry curvature (MBC), we establish an optical bound on the MBC for two-dimensional TRS insulators. By utilizing experimental data on the optical conductivity within a certain energy range, the topological signatures can be identified through the frequency integration of the optical bound. This is supported by the momentum integration of the refined TDI and its f -sum rule and topological extension, which provide a topological lower bound. Meanwhile, the decay of optical weight in the topologically trivial region can be controlled by the optical gap and the inverse mass tensor. We illustrate our approach using three representative topological models: the Kane-Mele model, mirror-protected insulator, and quadrupole insulator. Remarkably, we find that the quantized quantum volume (QV) in the mirror-protected insulator results from the Gauss-Bonnet theorem. Since QV has a topological lower bound, this suggests that double QV can be interpreted as an upper bound on the number of boundary states. Our findings offer a method for extracting the topological signatures of TRS insulators using optical conductivity data.

Introduction.—In the presence or absence of time-reversal symmetry, topological insulating phases can be categorized into two distinct groups: TRS phases and magnetic phases. The former group includes topological insulators (TIs) [1–3], topological crystalline insulators (TCIs) [4, 5], and higher-order topological insulators (HOTIs) [6]. When time-reversal symmetry is broken, the resulting phases include Chern insulators [7, 8] and fractional Chern insulators (FCIs) [9–19]. These time-reversal broken phases share a common characteristic: they possess a nonzero (fractional) Chern number. However, even when time-reversal symmetry is broken, there are topological phases that exhibit no bulk Chern number, such as axion insulators [20, 21] and antiferromagnetic topological insulators [22–24], whose topology is described by the θ -term [25] or Z_2 invariant [26]. Recently, several studies have focused on topological systems with a nonzero Chern number (or Euler number) [27–42]. All these works have proposed using optical circular dichroism measurements to probe the Chern number. However, in TRS systems with certain crystalline symmetries [43–45], there are no bulk Chern numbers or Berry curvature. How does topology emerge with the vanishing of Berry curvature, and how can it be probed through optical measurements? This remains elusive.

In this Letter, we establish a measurable optical bound derived from the refined TDI, which is related to the trace and determinant of the quantum metric and the MBC [46–48] in TRS systems. The optical bound provides a useful tool for experimentally identifying the topological signatures and probing the upper limit of MBC as a function of frequency in these systems. It is important to note that Berry curvature vanishes in the presence of both time-reversal symmetry and inversion symmetry (or mirror and rotational symmetry) [44]. To understand how the vanishing of Berry curvature relates to topology, we define the MBC by incorporating the absolute value symbol into the band summation in the expression for Berry

curvature, i.e.,

$$\bar{\Omega}_{ab}(\mathbf{k}) = \sum_{m \in \text{occ}} \sum_{n \in \text{unocc}} \bar{\Omega}_{ab}^{mn}(\mathbf{k}), \quad (1)$$

where $\bar{\Omega}_{ab}^{mn}(\mathbf{k}) = |-2\Im(r_{mn}^a(\mathbf{k})r_{nm}^b(\mathbf{k}))|$ and $r_{mn}^a(\mathbf{k}) = \langle u_m(\mathbf{k}) | i\partial_{k_a} | u_n(\mathbf{k}) \rangle$ is the interband Berry connection, and $a = x, y$. In most cases, the MBC does not vanish and is sensitive to broken crystalline symmetry, which lowers the value of the MBC.

Kubo-Greenwood formula.—The linear optical conductivity can be expressed by the Kubo-Greenwood formula [49–51]:

$$\sigma_{ab}(\omega) = \frac{e^2}{i\hbar} \sum_{m \neq n} \int \frac{d^2\mathbf{k}}{(2\pi)^2} \frac{f_{mn}(\mathbf{k})}{E_{mn}(\mathbf{k})} \frac{\mathcal{M}_{mn}^a(\mathbf{k})\mathcal{M}_{nm}^b(\mathbf{k})}{\hbar\omega + E_{mn}(\mathbf{k}) + i0^+}, \quad (2)$$

where the velocity matrix element $\mathcal{M}_{mn}^a(\mathbf{k}) = \langle u_m(\mathbf{k}) | \hbar\hat{v}_a | u_n(\mathbf{k}) \rangle$, $f_n(\mathbf{k}) = 1/[1 + e^{(E_n(\mathbf{k}) - \mu)/k_B T}]$ and $\hat{v}_a = \frac{1}{\hbar} \frac{\partial \hat{H}}{\partial k_a}$ are the Fermi-Dirac distribution function and velocity operator, respectively. We denote $f_{mn}(\mathbf{k}) = f_m(\mathbf{k}) - f_n(\mathbf{k})$ and $E_{mn}(\mathbf{k}) = E_m(\mathbf{k}) - E_n(\mathbf{k})$, where $H(\mathbf{k}) | u_n(\mathbf{k}) \rangle = E_n(\mathbf{k}) | u_n(\mathbf{k}) \rangle$. Here μ is the chemical potential. In the presence of interactions, one may directly replace $H(\mathbf{k})$, $E_n(\mathbf{k})$ and $u_n(\mathbf{k})$ with their many-body counterparts under twisted boundary conditions [36, 52–54] and then obtain the corresponding expressions for the optical conductivity and the quantum geometric tensor.

The real part of longitudinal optical conductivity corresponds to absorption, which is the primary focus of this work. The interband contribution to the real part of optical conduc-

tivity in the clean limit can be expressed as follows:

$$\Re\sigma_{aa}(\omega) = -\frac{\pi e^2}{\hbar} \sum_{m \neq n} \int \frac{d^2\mathbf{k}}{(2\pi)^2} \frac{f_{mn}(\mathbf{k})}{E_{mn}(\mathbf{k})} |\mathcal{M}_{mn}^a(\mathbf{k})|^2 \times \delta(\hbar\omega + E_{mn}(\mathbf{k})). \quad (3)$$

Since we consider the TRS systems, there is no optical Hall conductivity. To connect this with quantum geometry, we assume the system is at zero temperature and utilize the relationship between the velocity matrix element and the interband Berry connection, $\langle u_m(\mathbf{k}) | \hbar \hat{v}_a | u_n(\mathbf{k}) \rangle = i E_{mn} r_{mn}^a(\mathbf{k})$ where $m \neq n$, to express the real part of optical conductivity as

$$\Re\sigma_{aa}(\omega) = \pi e^2 \omega \sum_{m \neq n} \int \frac{d^2\mathbf{k}}{(2\pi)^2} r_{mn}^a r_{nm}^a \delta(\hbar\omega + E_{mn,\mathbf{k}}). \quad (4)$$

Furthermore, one can introduce the quantum geometric tensor [55–57], $Q_{ab}^{mn}(\mathbf{k}) = r_{mn}^a(\mathbf{k}) r_{nm}^b(\mathbf{k}) = g_{ab}^{mn}(\mathbf{k}) - \frac{i}{2} \Omega_{ab}^{mn}(\mathbf{k})$, where $g_{ab}^{mn}(\mathbf{k})$ and $\Omega_{ab}^{mn}(\mathbf{k})$ are the component of quantum metric and Berry curvature, respectively. Note that in linearly polarized optical responses, the term for Berry curvature is absent. Recall that there is no Berry curvature in TRS systems that possess inversion or other symmetries [45]. Finally, we can rewrite the absorption part of longitudinal conductivity as

$$\Re\sigma_{aa}(\omega) = \pi e^2 \omega \sum_{m \neq n} \int \frac{d^2\mathbf{k}}{(2\pi)^2} g_{aa}^{mn}(\mathbf{k}) \delta(\hbar\omega + E_{mn}(\mathbf{k})). \quad (5)$$

In this work, we mainly focus on a quantity, which we call optical bound, i.e.,

$$\mathcal{K}_{OP}(\omega) = \frac{2[\Re\sigma_{xx}(\omega) + \Re\sigma_{yy}(\omega)]}{\hbar\omega}, \quad (6)$$

whose frequency integration is given by $\mathcal{K}_{OP}^\infty = \frac{1}{2\pi} \int_0^\infty d\omega \mathcal{K}_{OP}(\omega)$, which contains the topological signatures provided by the Souza-Wilkens-Martin (SWM) sum rule [53], the refined TDI and its topological extension defined below. To reveal the behavior of the MBC, we introduce the corresponding imaginary part of the generalized (circularly polarized) optical Hall conductivity [36, 42, 58–60], i.e.,

$$\Im\bar{\sigma}_{xy}(\omega) = \frac{\pi e^2}{\hbar} \sum_{m \neq n} \int \frac{d^2\mathbf{k}}{(2\pi)^2} \bar{\Omega}_{xy}^{mn}(\mathbf{k}) \delta(\hbar\omega + E_{mn}(\mathbf{k})). \quad (7)$$

The magnitude of $\Im\bar{\sigma}_{xy}(\omega)$ is always lower than the optical bound, which we will study below.

Refined trace-determinant inequality.—The (refined) TDI serves as a foundational element for establishing the concept of optical bounds. It links geometric and topological information with experimental observables. To begin, we will first review the trace condition [62] in two dimensions:

$\text{tr}g(\mathbf{k}) \geq |\Omega(\mathbf{k})|$, where $\text{tr}g(\mathbf{k}) = g_{xx}(\mathbf{k}) + g_{yy}(\mathbf{k})$ is the trace of non-Abelian quantum metric [55, 63, 64], and $\Omega(\mathbf{k})$ is the non-Abelian Berry curvature. The TDI was first developed for flat Chern bands in lattice systems as a condition to satisfy the Girvin-MacDonald-Platzman algebra [65] of projected density operators to all orders, with the aim of realizing FCI phases [9–12]. When the trace condition is saturated, the FCI phases can be achieved in lattice systems. Since we consider the TRS systems, both the Berry curvature and the Chern number are zero. The determinant condition [62, 66], i.e., $\sqrt{\det(g(\mathbf{k}))} \geq |\Omega(\mathbf{k})|/2$, does not yield useful information. Instead, to combine the two conditions, we propose the following refined TDI:

$$\text{tr}g(\mathbf{k}) \geq 2\sqrt{\det(g(\mathbf{k}))} \geq \bar{\Omega}_{ab}(\mathbf{k}). \quad (8)$$

where $\bar{\Omega}_{ab}(\mathbf{k})$ is the MBC characterizing the nontrivial topology of a TRS system. Note that $\bar{\Omega}_{ab}(\mathbf{k}) \geq |\Omega_{ab}(\mathbf{k})|$. Crucially, based on the semi-positive definite property of the quantum metric, this refined TDI holds for arbitrary quantum states in two dimensions. When we integrate the refined TDI both sides, the inequality becomes:

$$\int \frac{d^2\mathbf{k}}{2\pi} \text{tr}g(\mathbf{k}) \geq \int \frac{d^2\mathbf{k}}{2\pi} 2\sqrt{\det(g(\mathbf{k}))} \geq \int \frac{d^2\mathbf{k}}{2\pi} \bar{\Omega}_{ab}(\mathbf{k}). \quad (9)$$

In the following discussion, we denote the above integrated TDI as $\mathcal{K} \geq 2\mathcal{V} \geq \bar{\mathcal{C}}$. Importantly, \mathcal{K} called quantum weight can be observed through optical responses, whereas \mathcal{V} and $\bar{\mathcal{C}}$ represents the QV [67–70] and “pseudo-Chern number” of the occupied bands, respectively. Note that after multiplying by the normalized constant $\frac{1}{2\pi}$, the QV has a transparent physical interpretation. Recall that in TRS systems, such as TIs, TCIs, and HOTIs, there is no bulk Chern number; however, a nonzero $\bar{\mathcal{C}}$ can still exist and will be slightly larger than or equal to the number of boundary states if there is no term breaking certain crystalline symmetry. To reveal the topological information when $\bar{\mathcal{C}}$ is smaller than the number of boundary states, a topological lower bound is introduced using the projection method [71–76], which will be studied below.

According to the Gauss-Bonnet theorem [77, 78] (see End Matter (EM)), there exists a correspondence between QV and topological invariants for certain manifolds [67, 78]. This suggests that the quantized QV can be regarded as a geometric invariant under certain conditions [78] (see Fig. 1(d2) and EM). However, Figs. 1(d1) and 2(d1,d2) show that QV exhibits slight variations when the parameters are altered, indicating that it cannot be generally quantized. The variation of the quantum geometric quantities during the topological deformation is constrained by the “topological” inequality [36, 79]:

$$\frac{\pi e^2}{2} \frac{\mathcal{M}}{E_g} \geq \mathcal{K} \geq 2\mathcal{V} \geq \bar{\mathcal{C}} \geq \sum_{s=1}^{\text{sec}} |\mathcal{N}_s| \quad (10)$$

where $\mathcal{M} = \sum_{m,n,a} \int \frac{d\mathbf{k}}{(2\pi)^2} [M_{mn}^{-1}(\mathbf{k})]_{aa} \langle c_{\mathbf{k}m}^\dagger c_{\mathbf{k}n} \rangle$ and $[M_{mn}^{-1}(\mathbf{k})]_{aa} = \sum_{\alpha\beta} U_{m,\alpha}^\dagger(\mathbf{k}) \frac{\partial^2 H_{\alpha\beta}(\mathbf{k})}{\partial(\hbar k_a)^2} U_{\beta,n}(\mathbf{k})$ is the inverse mass tensor [49, 80]. The topological number \mathcal{N}_s will

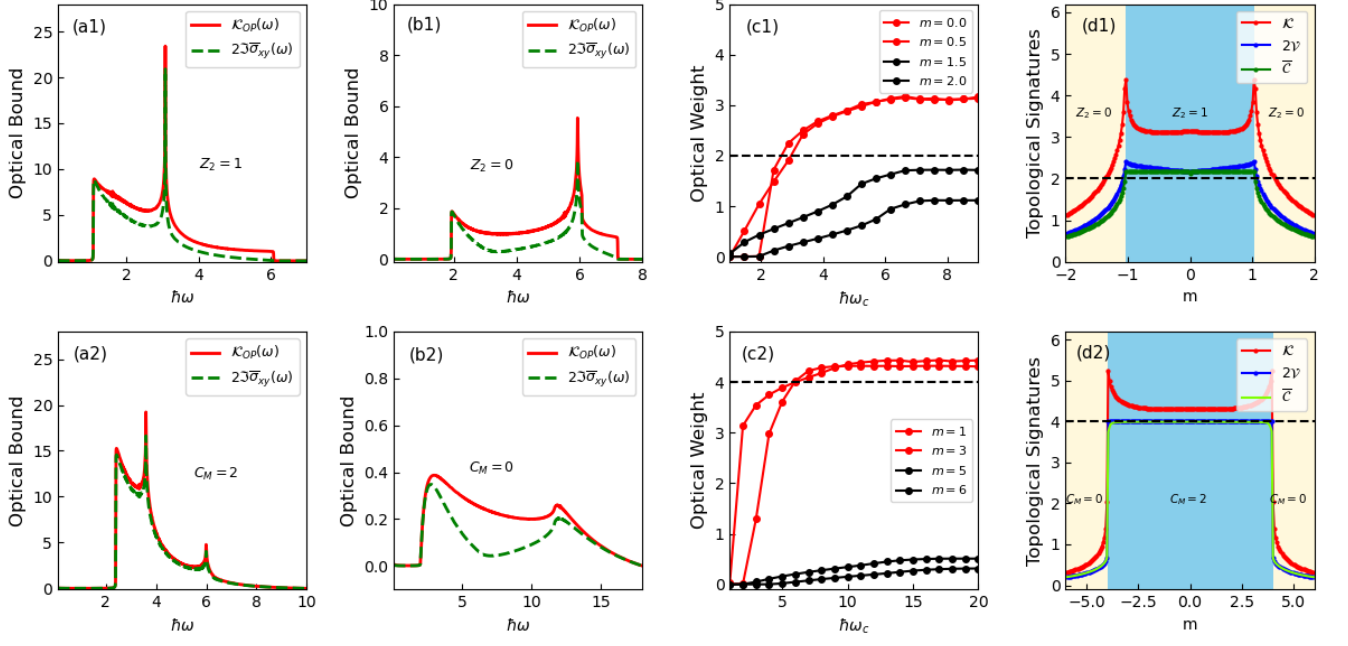


FIG. 1. Optical bound, optical weight, and topological signatures of the Kane-Mele model and TCI model of mirror-protected insulator. (a1, a2, b1, b2) The optical bound as a function of frequency with $\lambda_v = 0.5t, 2t$ in (a1,b1) and $v_m = 1, 5$ in (a2,b2). The red solid (green dashed) line represents the optical bound (generalized optical Hall conductivity) in the nontrivial (a1, a2) and trivial phases (b1, b2). (c1, c2) The optical weight $\mathcal{K}_{OP}^{\omega_c}$ as a function of frequency cutoff for four parameters. The red (black) lines correspond to the nontrivial (trivial) phase. (d1, d2) The topological signatures \mathcal{K} , $2\mathcal{V}$ and \overline{C} as a function of a range of parameters. The back dashed line represents the number of boundary states. We calculate $\Re\sigma_{aa}$ and $\Im\overline{\sigma}_{ab}$ in units of e^2/h . Here, we set $(t, \lambda_{SO}, \lambda_R, \lambda_v) = (1, 0.2t, 0, m)$ and $(t_1, t_2, t_{PH}, v_s, v_m) = (2, 1.5, 0.1, 1.3, m)$ for the Kane-Mele model and TCI [61], respectively.

be defined below [81]. Here E_g is the optical gap [36]. In other words, the optical gap and the degree of flatness [82], which relates to the inverse mass tensor [36, 79], are the two key factors controlling the variation of the quantum weight and quantum volume. We find that crystalline symmetry also plays a significant role (see below and EM).

In TRS systems, the total Chern number of the occupied bands is always zero. However, one can project the occupied bands onto different topological sections. Consequently, the integrated TDI Eq. (9) is adapted as follows:

$$\mathcal{K} \geq 2\mathcal{V} \geq \overline{C} \geq \sum_{s=1}^{sec} |\mathcal{N}_s|, \quad (11)$$

where \mathcal{N}_s represents the topological number in different sections (see SM [79] for more details). For instance, one can utilize the spin projection operator, $P(\mathbf{k})\hat{s}P(\mathbf{k})$ [72–76], to separate the occupied bands into spin-up and spin-down sections, each of which has a defined Chern number. Here $P(\mathbf{k})$ is the projection operator of occupied bands and \hat{s} is the (pseudo) spin operator. As a result, \mathcal{N}_s becomes the spin Chern number C_{\pm} [72–76] in the case of TIs/TCIs. It is important to note that the quantum metric is a robust geometric quantity that is always non-vanishing. In contrast, topological invariants such as the Chern number and the Z_2 invariant vanish in TIs and HOTIs, respectively, and cannot be measured directly.

Fortunately, by utilizing data from optical response measurements—specifically, the optical bound—one can obtain topological signals, which we will explore further below.

Optical Bound.—In the previous subsection, we discussed the refined TDI and the “topological” inequality. Now, we will examine their relationship with optical responses and reveal their topological signatures. By utilizing the identities $r_{mn}^a = \hbar v_{mn}^a / (iE_{mn})$ and $|v_{mn}^x \pm iv_{mn}^y|^2 = |v_{mn}^x|^2 + |v_{mn}^y|^2 \mp i(v_{mn}^x v_{nm}^y - v_{mn}^y v_{nm}^x)$ which is always semi-positive [83], and by applying the TDI, we can derive the optical bound on the components of the MBC for any interband transition contour (see SM [79]), i.e.,

$$\frac{\Re\sigma_{mn}^{xx}(\mathbf{k}, \omega) + \Re\sigma_{mn}^{yy}(\mathbf{k}, \omega)}{\hbar\omega} \geq \Im\overline{\sigma}_{mn}^{xy}(\mathbf{k}, \omega), \quad (12)$$

where we define $\Re\sigma_{mn}^{aa}(\mathbf{k}, \omega) = c|v_{mn}^{aa}|^2\delta(\omega + \omega_{mn})/|\omega_{mn}|$, and $\Im\overline{\sigma}_{mn}^{xy}(\mathbf{k}, \omega) = c|-2\Im(v_{mn}^x v_{nm}^y / \omega_{mn}^2)|\delta(\omega + \omega_{mn})$. The constant, $c = \pi e^2 / \hbar$. The corresponding real or imaginary part of $\sigma_{mn}^{ab}(\mathbf{k}, \omega)$ which are not considered in this study, can also be defined.

After integrating the momentum variable and performing the band summation, we ultimately obtain the optical bound on MBC at any frequency,

$$\mathcal{K}_{OP}(\omega) \geq 2\Im\overline{\sigma}_{xy}(\omega). \quad (13)$$

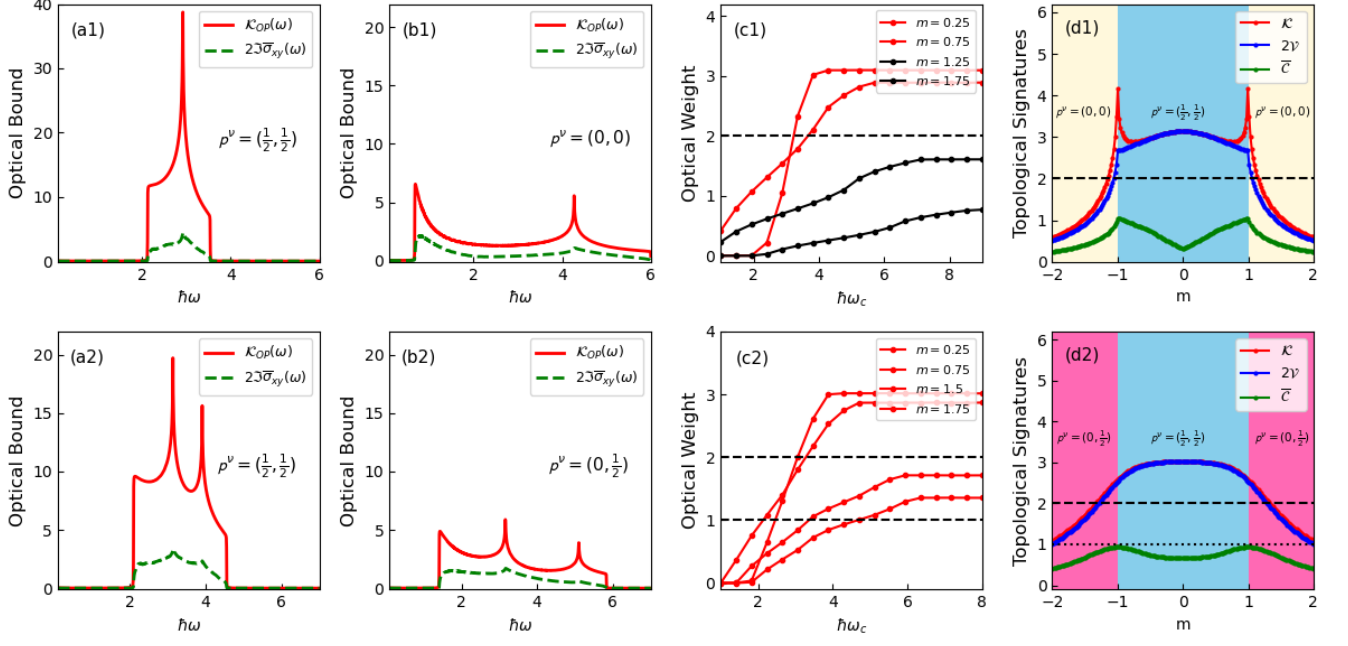


FIG. 2. Optical bounds, optical weight, and topological signatures of HOTI model of quadrupole insulator. (a1, a2, b1, b2) The optical bound as a function of frequency. The red solid (green dashed) line represents the optical bound (generalized optical Hall conductivity). In (a1, b1) and (a2, b2), we set $(\gamma_x, \gamma_y) = (0.25, 0.25), (1.25, 1.25)$ and $(\gamma_x, \gamma_y) = (0.25, 0.5), (1.5, 0.5)$, respectively. (c1, c2) The optical weight $\mathcal{K}_{OP}^{\omega_c}$ as a function of frequency cutoff for four parameters. The red (black) line corresponds to the nontrivial (trivial) phase. (d1, d2) The topological signatures \mathcal{K} , $2\mathcal{V}$, and $\bar{\mathcal{C}}$ as a function of a range of parameters. The black dashed and dotted lines represent the number of boundary states in the phases $\mathbf{p}^\nu = (\frac{1}{2}, \frac{1}{2})$ and $\mathbf{p}^\nu = (0, \frac{1}{2})$, respectively. We calculate $\Re\sigma_{aa}$ and $\Im\bar{\sigma}_{ab}$ in units of e^2/h . We take $(\gamma_x, \gamma_y) = (m, m)$ for panels (c1,d1) and $(\gamma_x, \gamma_y) = (m, 0.5)$ for panels (c2,d2), respectively. Here, we set $(\lambda_x, \lambda_y) = (1, 1)$.

Here, we multiply both side of 2 to maintain consistency with the definitions of quantum geometry and topology. Importantly, the left-hand term, which we refer to as the optical bound, can be obtained through measurements of optical responses. In contrast, the right-hand term represents the corresponding generalized optical Hall conductivity. To identify the range of frequencies that contribute to the topological signatures, we can calculate the optical weight as a function of the frequency cutoff ω_c : $\mathcal{K}_{OP}^{\omega_c} = \frac{1}{2\pi} \int_0^{\omega_c} d\omega \mathcal{K}_{OP}(\omega)$. By combining the two formulas $\mathcal{K}_{OP}^{\infty} = \frac{e^2}{h} \mathcal{K}$ (see SM [79]) and $\mathcal{K} \geq 2\mathcal{V} \geq \bar{\mathcal{C}} \geq \sum_{s=1}^{sec} |N_s|$, one can extract the topological signals from the optical weight $\mathcal{K}_{OP}^{\omega_c}$ if the quantum weight decays rapidly in the topologically trivial region. As a result, if the optical weight $\mathcal{K}_{OP}^{\omega_c}$ is larger than the number of boundary states, it carries topological information. For example, the number of boundary states is $|C_+| + |C_-|$ in the case of TIs.

Models and results.—To reveal the topological and geometric information of the optical bound and TDI, we examine three typical TRS models: the Kane-Mele model, mirror-protected insulator, and quadrupole insulator. First, we consider the Kane-Mele model [84], whose Hamiltonian is given by

$$H(\mathbf{k}) = \sum_{a=1}^5 d_a(\mathbf{k})\Gamma^a + \sum_{a<b=1}^5 d_{ab}(\mathbf{k})\Gamma^{ab} \quad (14)$$

where $d_1 = t(1 + 2\cos(x)\cos(y))$, $d_2 = \lambda_v$, $d_3 = \lambda_R(1 - \cos(x)\cos(y))$, $d_4 = -\sqrt{3}\lambda_R\sin(x)\sin(y)$, $d_{12} = -2t\cos(x)\sin(y)$, $d_{15} = \lambda_{SO}(2\sin(2x) - 4\sin(x)\cos(y))$, $d_{23} = -\lambda_R\cos(x)\sin(y)$ and $d_{24} = \sqrt{3}\lambda_R\sin(x)\cos(y)$ with $x = k_x/2$ and $y = \sqrt{3}k_y/2$. The Dirac matrices are $\Gamma^{(1,2,3,4,5)} = (\tau_x\sigma_0, \tau_z\sigma_0, \tau_y\sigma_x, \tau_y\sigma_y, \tau_y\sigma_z)$, and $\Gamma^{ab} = [\Gamma^a, \Gamma^b]/(2i)$, where the Pauli matrices $\tau_k(\sigma_k)$ represent the sublattice (spin) degree of freedom. Note that the term $d_2\Gamma^2$ breaks inversion symmetry and induces a topological phase transition.

Fig. 1(a1,b1) shows the optical bounds in the nontrivial and trivial phases, respectively. As shown in Fig. 1(c1), the optical weight with $m = 0$ (and $0.5t$) saturates to a value greater than 2 after a certain frequency cutoff. This indicates that the phase is nontrivial. Because Kane-Mele model hosts C_3 rotation symmetry, the optical bound decays very slowly after the transition to the trivial phase. Fortunately, the decay can be significantly enhanced by increasing the optical gap, which is controlled by λ_{SO} (see End Matter). The optical weight and QV cannot represent the Z_2 invariant. Instead, they reflect the topological information related to bulk-boundary correspondence [85], which describes the relationship between the bulk topological invariant of a gapped system and the number of topologically protected boundary states. As shown in Fig. 1(d1), the double QV consistently exceeds 2 in the nontrivial region, it suggests that the double QV can be interpreted as the

tightly upper bound on the number of boundary states. If the Hamiltonian preserves the symmetry of the lattice, \bar{C} will be slightly larger than 2, as is the case for TIs. The Rashba term, which breaks the M_z mirror symmetry, serves a gap-closing role and mixes spin up and down states, which can lower the value of \bar{C} (see End Matter Fig. 3(b1)). Note that C_6 rotation symmetry also makes the optical bound decay slowly upon transitioning to the trivial phase. In other words, the quantum metric elements g_{ab} are highly anisotropic. However, if C_4 rotation symmetry is present, the degree of anisotropy can be significantly reduced, as we will demonstrate in the cases of TCI and HOTI below.

Next, we consider the TCI model of mirror-protected insulator [61]:

$$\begin{aligned} H(\mathbf{k}) = & t_1 \tau_z \sigma_0 [\cos(k_x) + \cos(k_y)] \\ & + t_2 \tau_x \sigma_0 [\cos(k_x) - \cos(k_y)] \\ & + t_{PH} \tau_0 \sigma_0 [\cos(k_x) + \cos(k_y)] \\ & + v_s \tau_y \sigma_z \sin(k_x) \sin(k_y) + v_m \tau_z \sigma_0 \end{aligned} \quad (15)$$

where $\tau(\sigma)$ corresponds to the s and d-orbital (spin) degrees of freedom, it is invariant under the symmetries of the layer group $p4/mmm1'$ (see [61]'s Table 1). Due to the presence of the mirror symmetry M_z , the topology of the TCI model is characterized by the mirror Chern number $C_{M_z} = 2$ [61].

The optical bounds of the TCI model are shown in Fig. 1 (a2, b2). Furthermore, the optical weight rapidly saturates to a value greater than 4 as the frequency cutoff increases in the nontrivial phase, while the optical weight remains low in the trivial phase. Notably, as shown in Fig. 1(d2), \mathcal{V} is quantized. This is the result of the TCI Hamiltonian hosting C_4 rotation symmetry and all matrix elements having even functions, as well as the Gauss-Bonnet theorem [77, 78]. Therefore, the topology can also be characterized by the Euler number [78] (see End Matter). Due to the presence of C_4 rotation symmetry, \mathcal{K} , \mathcal{V} , and \bar{C} rapidly decay and reach nearly the same value in the trivial and nontrivial phases, respectively, reflecting the near overlap between the optical bound and the generalized optical Hall conductivity.

Lastly, we consider the HOTI model of quadrupole insulator [86, 87]:

$$\begin{aligned} H(\mathbf{k}) = & [\gamma_x + \lambda_x \cos(k_x)] \Gamma_4 + \lambda_x \sin(k_x) \Gamma_3 \\ & + [\gamma_y + \lambda_y \cos(k_y)] \Gamma_2 + \lambda_y \sin(k_y) \Gamma_1, \end{aligned} \quad (16)$$

where $\Gamma_0 = \tau_3 \otimes \tau_0$, $\Gamma_k = -\tau_2 \otimes \tau_k$ ($k = 1, 2, 3$), $\Gamma_4 = \tau_1 \otimes \tau_0$, $\tau_{1,2,3}$ represent the Pauli matrices, while τ_0 is the 2×2 identity matrix. The model exhibits a quadrupole phase, $q_{xy} = 1/2$, with helical corner states when the parameters satisfy $\gamma_x/\lambda_x \in (-1, 1)$ and $\gamma_y/\lambda_y \in (-1, 1)$.

As shown in Fig. 2 (a1, a2), unlike the case of TCI, the optical bound and the generalized optical Hall conductivity are well separated in the nontrivial phase. This feature reflects on the larger difference between $2\mathcal{V}$ and \bar{C} . The topological signatures can be identified in Fig. 2 (c1, c2), where the optical weight is always greater than 2 for $m \in (-1, 1)$. Fig. 2 (d1)

shows both \mathcal{K} and $2\mathcal{V}$ exhibit discontinuous behavior [88–90] and nearly overlap, reflecting a topological phase transition from $\mathbf{p}^\nu = (1/2, 1/2)$ to $\mathbf{p}^\nu = (0, 0)$, characterized by band gap closing. In contrast, as shown in Fig. 2 (d2), a different type of topological phase transition from $\mathbf{p}^\nu = (1/2, 1/2)$ to $\mathbf{p}^\nu = (0, 1/2)$ occurs without gap closing, where both \mathcal{K} and $2\mathcal{V}$ display continuous behavior and nearly overlap. Note that in the phase with $\mathbf{p}^\nu = (0, 1/2)$, there is only one boundary state at the corners.

Discussions.—The refined TDI is particularly useful for systems that host completely flat bands, such as fractional quantum spin Hall insulator (FQSHI) [91–96]. It is known that when the TDI is saturated, the FCI phase can be realized [62, 97]. In TRS systems, when the TDI is saturated, i.e., $\mathcal{K} = 2\mathcal{V} = \bar{C} = |C_+| + |C_-|$ [36, 52, 98], we expect that the FQSHI phase can emerge. This suggests that "pseudo-Chern number" can be quantized. Since the TDI can also be applied to systems with broken TRS, in this case, we have $\text{tr}g(\mathbf{k}) = 2\sqrt{\det(g(\mathbf{k}))} = \Omega_{ab}(\mathbf{k}) = |\Omega_{ab}(\mathbf{k})|$. This indicates that all components of the Berry curvature will be semi-positive (semi-negative) or entirely positive (negative) in the FCI phases [99, 100]. In other words, the imaginary part of the circularly polarized optical Hall conductivity will also be semi-positive (semi-negative) or entirely positive (negative).

Conclusions.—In summary, by focusing on two-dimensional TRS insulators, we have established a solid foundation and provided numerical demonstrations of how topological signatures can be identified through measurements of longitudinal optical responses. The optical weight and QV sets an upper limit on the number of boundary states. The close relationship between geometry and topology, as revealed by the integrated TDI, is experimentally detectable. Remarkably, we found that the QV can be exactly quantized in certain types of TCIs [61]. This is a result of the Gauss-Bonnet theorem [77, 78], which is formulated using a new expression. These concepts can also be applied to systems that break time-reversal symmetry, particularly in Moiré materials hosting flat Chern bands [95]. Our work opens a new avenue for probing the topology and possible (nearly) quantization in quantum geometry through measurements of optical responses. In future investigations, it is important to rule out whether other factors, such as disorder [101], charge-density waves, spin-density waves, and many-body effects [102], may cause the optical bound to be greater than a certain integer while belonging to a topologically trivial phase.

Acknowledgments The author thanks Hsiu-Chuan Hsu for providing the cluster for parallel numerical computation. The author is grateful to Ming-Che Chang for reading the manuscript and providing insightful comments. The author also thanks Po-Yao Chang, Hsiu-Chuan Hsu, and Jih-Shih You for useful discussions. P.M.C. was supported by the post-doctoral fellowship of the Ministry of Science and Technology (MOST) in Taiwan under grant no. MOST 111-2636-M-007-003 and 111-2811-M-004-001.

Note added: After the submission, the author became aware

of two works, Refs. [103, 104], which study the Z_2 bound using the Wilson loop and the quantum geometric bounds using the spin projection operator, respectively, for time-reversal symmetric insulators. The author thanks Robert-Jan Slager for communicating his unpublished work.

* pmchiu2022@gmail.com

- [1] M. Z. Hasan and C. L. Kane, Colloquium: Topological insulators, *Rev. Mod. Phys.* **82**, 3045 (2010).
- [2] X.-L. Qi and S.-C. Zhang, Topological insulators and superconductors, *Rev. Mod. Phys.* **83**, 1057 (2011).
- [3] Y. Ando, Topological insulator materials, *J. Phys. Soc. Jpn.* **82**, 102001 (2013).
- [4] Y. Ando and L. Fu, Topological crystalline insulators and topological superconductors: From concepts to materials, *Annu. Rev. Condens. Matter Phys.* **6**, 361 (2015).
- [5] C.-K. Chiu et al., Classification of topological quantum matter with symmetries, *Rev. Mod. Phys.* **88**, 035005 (2016).
- [6] Y.-B. Yang, J.-H. Wang, K. Li, and Y. Xu, Higher-order topological phases in crystalline and non-crystalline systems: a review, *J. Phys.: Condens. Matter* **36**, 283002 (2024).
- [7] F. D. M. Haldane, Model for a quantum hall effect without landau levels: Condensed-matter realization of the parity anomaly, *Phys. Rev. Lett.* **61**, 2015 (1988).
- [8] C.-Z. Chang, C.-X. Liu, and A. H. MacDonald, Colloquium: Quantum anomalous hall effect, *Rev. Mod. Phys.* **95**, 011002 (2023).
- [9] S. A. Parameswaran, R. Roy, and S. L. Sondhi, Fractional quantum hall physics in topological flat bands, *Comptes Rendus Physique* **14**, 816 (2013).
- [10] E. J. Bergholtz and Z. Liu, *Int. J. Mod. Phys. B* **27**, 1330017 (2013).
- [11] T. Neupert, C. Chamon, T. Iadecola, L. H. Santos, and C. Mudry, Fractional (chern and topological) insulators, *Phys. Scr.* **T164**, 014005 (2015).
- [12] Z. Liu and E. J. Bergholtz, *Encyclopedia of Condensed Matter Physics, Second Edition, Vol. 1* (Elsevier Ltd., 2024) p. 515.
- [13] H. Park et al., Observation of fractionally quantized anomalous hall effect, *Nature* **622**, 74 (2023).
- [14] J. Cai et al., Signatures of fractional quantum anomalous hall states in twisted mote2, *Nature* **622**, 63 (2023).
- [15] Y. Zeng et al., Thermodynamic evidence of fractional chern insulator in moiré mote2, *Nature* **622**, 69 (2023).
- [16] F. Xu et al., Observation of integer and fractional quantum anomalous hall effects in twisted bilayer mote2, *Phys. Rev. X* **13**, 031037 (2023).
- [17] Z. Ji et al., Local probe of bulk and edge states in a fractional chern insulator, *Nature* **635**, 578 (2024).
- [18] E. Anderson et al., Trion sensing of a zero-field composite fermi liquid, *Nature* **635**, 590 (2024).
- [19] E. Redekop et al., Direct magnetic imaging of fractional chern insulators in twisted mote2, *Nature* **635**, 584 (2024).
- [20] D. M. Neno, C. A. C. Garcia, J. Gooth, C. Felser, and P. Narang, Axion physics in condensed-matter systems, *Nat. Rev. Phys.* **2**, 682 (2020).
- [21] A. Sekine and K. Nomura, Axion electrodynamics in topological materials, *J. Appl. Phys.* **129**, 141101 (2021).
- [22] Y. Tokura, K. Yasuda, and A. Tsukazaki, Magnetic topological insulators, *Nat. Rev. Phys.* **1**, 126 (2019).
- [23] P. Wang, J. Ge, J. Li, Y. Liu, Y. Xu, and J. Wang, Intrinsic magnetic topological insulators, *The Innovation* **2**, 100098 (2021).
- [24] B. A. Bernevig, C. Felser, and H. Beidenkopf, Progress and prospects in magnetic topological materials, *Nature* **603**, 41 (2022).
- [25] X.-L. Qi, T. L. Hughes, and S.-C. Zhang, Topological field theory of time-reversal invariant insulators, *Phys. Rev. B* **78**, 195424 (2008).
- [26] R. S. K. Mong, A. M. Essin, and J. E. Moore, Antiferromagnetic topological insulators, *Phys. Rev. B* **81**, 245209 (2010).
- [27] D. T. Tran, A. Dauphin, A. G. Grushin, P. Zoller, and N. Goldman, Probing topology by heating: Quantized circular dichroism in ultracold atoms, *Sci. Adv.* **3**, e1701207 (2017).
- [28] T. Ozawa and N. Goldman, Extracting the quantum metric tensor through periodic driving, *Phys. Rev. B* **97**, 201117 (2018).
- [29] C. Repellin and N. Goldman, Detecting fractional chern insulators through circular dichroism, *Phys. Rev. Lett.* **122**, 166801 (2019).
- [30] O. Pozo, C. Repellin, and A. G. Grushin, Quantization in chiral higher order topological insulators: Circular dichroism and local chern marker, *Phys. Rev. Lett.* **123**, 247401 (2019).
- [31] T. Ozawa and N. Goldman, Probing localization and quantum geometry by spectroscopy, *Phys. Rev. Research* **1**, 032019(R) (2019).
- [32] W. J. Jankowski, A. S. Morris, A. Bouhon, F. N. Ünal, and R.-J. Slager, Optical manifestations of topological euler class in electronic materials, *arXiv:2311.07545* (2023).
- [33] M. Lysne, M. Schüler, and P. Werner, Quantum optics measurement scheme for quantum geometry and topological invariants, *Phys. Rev. Lett.* **131**, 156901 (2023).
- [34] A. Kruchkov and S. Ryu, Measure of an ultranarrow topological gap via quantum noise, *Phys. Rev. B* **110**, L041118 (2024).
- [35] A. Kruchkov and S. Ryu, Spectral sum rules reflect topological and quantum-geometric invariants, *arXiv:2312.17318* (2023).
- [36] Y. Onishi and L. Fu, Fundamental bound on topological gap, *Phys. Rev. X* **14**, 011052 (2024).
- [37] B. Ghosh, Y. Onishi, S.-Y. Xu, H. Lin, L. Fu, and A. Bansil, Probing quantum geometry through optical conductivity and magnetic circular dichroism, *arXiv:2401.09689* (2024).
- [38] I. Komissarov, T. Holder, and R. Queiroz, The quantum geometric origin of capacitance in insulators, *Nat. Commun.* **15**, 4621 (2024).
- [39] N. Verma and R. Queiroz, Instantaneous response and quantum geometry of insulators, *arXiv:2403.07052* (2024).
- [40] N. Verma and R. Queiroz, Quantum metric in step response, *arXiv:2406.17845* (2024).
- [41] W.-X. Qiu and F. Wu, Quantum geometry probed by chiral excitonic optical response of chern insulators, *arXiv:2407.03317* (2024).
- [42] S.-K. Bac et al., Probing berry curvature in magnetic topological insulators through resonant infrared magnetic circular dichroism, *Phys. Rev. Lett.* **134**, 016601 (2025).
- [43] D. Xiao, M.-C. Chang, and Q. Niu, Berry phase effects on electronic properties, *Rev. Mod. Phys.* **82**, 1959 (2010).
- [44] C. Fang, M. J. Gilbert, and B. A. Bernevig, Bulk topological invariants in noninteracting point group symmetric insulators, *Phys. Rev. B* **86**, 115112 (2012).
- [45] C. Ortix, Nonlinear hall effect with time-reversal symmetry: Theory and material realizations, *Adv. Quantum Technol.* **4**, 2100056 (2021).
- [46] One can define the MBC using the Hardy–Littlewood maximal function. In this work, we choose a simpler approach.
- [47] G. H. Hardy and J. E. Littlewood, A maximal theorem with function-theoretic applications, *Acta Math.* **54**, 81 (1930).

- [48] L. Grafakos, Classical and Modern Fourier Analysis (Pearson Education, Inc., 2004).
- [49] R. Kubo, Statistical-mechanical theory of irreversible processes. i. general theory and simple applications to magnetic and conduction problems, *J. Phys. Soc. Jpn.* **12**, 570 (1957).
- [50] D. A. Greenwood, The boltzmann equation in the theory of electrical conduction in metals, *Proc. Phys. Soc.* **71**, 585 (1958).
- [51] K.-E. Huhtinen and P. Törmä, Conductivity in flat bands from the kubo-greenwood formula, *Phys. Rev. B* **108**, 155108 (2023).
- [52] Q. Niu, D. J. Thouless, and Y.-S. Wu, Quantized hall conductance as a topological invariant, *Phys. Rev. B* **31**, 3372 (1985).
- [53] I. Souza, T. Wilkens, and R. M. Martin, Polarization and localization in insulators: Generating function approach, *Phys. Rev. B* **62**, 1666 (2000).
- [54] R. Resta, Electron localization in the quantum hall regime, *Phys. Rev. Lett.* **95**, 196805 (2005).
- [55] J. Ahn, G.-Y. Guo, and N. Nagaosa, Low-frequency divergence and quantum geometry of the bulk photovoltaic effect in topological semimetals, *Phys. Rev. X* **10**, 041041 (2020).
- [56] J. Ahn, G.-Y. Guo, N. Nagaosa, and A. Vishwanath, Riemannian geometry of resonant optical responses, *Nat. Phys.* **18**, 290 (2022).
- [57] R. Resta, The insulating state of matter: a geometrical theory, *Eur. Phys. J. B* **79**, 121 (2011).
- [58] H. Ebert, Magneto-optical effects in transition metal systems, *Rep. Prog. Phys.* **59**, 1665 (1996).
- [59] P. M. Oppeneer, Magneto-optical spectroscopy in the valence-band energy regime: relationship to the magnetocrystalline anisotropy, *J. Magn. Magn. Mater.* **188**, 275 (1998).
- [60] M. Gradhand, K. I. Wysokinski, J. F. Annett, and B. L. Györfy, Kerr rotation in the unconventional superconductor Sr_2RuO_4 , *Phys. Rev. B* **88**, 094504 (2013).
- [61] B. J. Wieder, Z. Wang, J. Cano, X. Dai, L. M. Schoop, B. Bradlyn, and B. A. Bernevig, Strong and fragile topological dirac semimetals with higher-order fermi arcs, *Nat. Commun.* **11**, 627 (2020).
- [62] R. Roy, Band geometry of fractional topological insulators, *Phys. Rev. B* **90**, 165139 (2014).
- [63] A. T. Rezaekhani, D. F. Abasto, D. A. Lidar, and P. Zanardi, Intrinsic geometry of quantum adiabatic evolution and quantum phase transition, *Phys. Rev. A* **82**, 012321 (2010).
- [64] Y.-Q. Ma, S. Chen, H. Fan, and W.-M. Liu, Abelian and non-abelian quantum geometric tensor, *Phys. Rev. B* **81**, 245129 (2010).
- [65] S. M. Girvin, A. H. MacDonald, and P. M. Platzman, Magneto-roton theory of collective excitations in the fractional quantum hall effect, *Phys. Rev. B* **33**, 2481 (1986).
- [66] Note that the determinant of the quantum metric should be semi-positive. We enforce this property by taking the absolute value of the determinant of the quantum metric in our calculations.
- [67] M. Gromov, Volume and bounded cohomology, *Publications Mathématiques de l'IHÉS* **56**, 5 (1982).
- [68] B. Mera and T. Ozawa, Kähler geometry and chern insulators: Relations between topology and the quantum metric, *Phys. Rev. B* **104**, 045104 (2021).
- [69] T. Ozawa and B. Mera, Relations between topology and the quantum metric for chern insulators, *Phys. Rev. B* **104**, 045103 (2021).
- [70] B. Mera and T. Ozawa, Engineering geometrically flat chern bands with fubini-study kähler structure, *Phys. Rev. B* **104**, 115160 (2021).
- [71] S. Kivelson, Wannier functions in one-dimensional disordered systems: Application to fractionally charged solitons, *Phys. Rev. B* **26**, 4269 (1982).
- [72] E. Prodan, Robustness of the spin-chern number, *Phys. Rev. B* **80**, 125327 (2009).
- [73] E. Prodan, Non-commutative tools for topological insulators, *New J. Phys.* **12**, 065003 (2010).
- [74] Y. Yang, Z. Xu, L. Sheng, B. Wang, D. Y. Xing, and D. N. Sheng, Time-reversal-symmetry-broken quantum spin hall effect, *Phys. Rev. Lett.* **107**, 066602 (2011).
- [75] S. Li, H.-C. Li, Y.-Y. Yang, D.-N. Sheng, and D.-Y. Xing, Spin chern numbers and time-reversal-symmetry-broken quantum spin hall effect, *Chin. Phys. B* **22**, 067201 (2013).
- [76] K.-S. Lin, G. Palumbo, Z. Guo, Y. Hwang, J. Blackburn, D. P. Shoemaker, F. Mahmood, Z. Wang, G. A. Fiete, B. J. Wieder, and B. Bradlyn, Spin-resolved topology and partial axion angles in three-dimensional insulators, *Nat. Commun.* **15**, 550 (2024).
- [77] S.-S. Chern, W. Chen, and K. S. Lam, Lectures on differential geometry (World Scientific Publishing Co. Pte. Ltd., 1999).
- [78] J. G. Ratcliffe, Foundations of Hyperbolic Manifolds (Springer Nature Switzerland AG, 2019).
- [79] See Supplemental Material at [URL will be inserted by publisher] for detailed discussions of i) quantum geometry, ii) refined trace-determinant inequality, iii) optical bound, iv) SWM sum rule and the relation between optical bound and quantum weight, v) upper bound of the quantum weight and the optical gap, vi) numerical results on band structure and quantum weight.
- [80] T. Hazra, N. Verma, and M. Randeria, Bounds on the superconducting transition temperature: Applications to twisted bilayer graphene and cold atoms, *Phys. Rev. X* **9**, 031049 (2019).
- [81] Note that the topological number \mathcal{N}_s is nonzero only in special bases, and we have $\bar{C} > \sum_{s=1}^{sec} \mathcal{N}_s$ or $\bar{C} < \sum_{s=1}^{sec} \mathcal{N}_s$ depending on whether certain crystalline symmetry is broken (see [79]). However, the quantum weight and the quantum volume are the same in any basis.
- [82] P. M. Chiu, Optical signatures of band flatness and anisotropic quantum geometry in magic-angle twisted bilayer graphene, *arXiv:2508.18152* (2025).
- [83] S. Sekh and I. Mandal, Circular dichroism as a probe for topology in three-dimensional semimetals, *Phys. Rev. B* **105**, 235403 (2022).
- [84] C. L. Kane and E. J. Mele, z_2 topological order and the quantum spin hall effect, *Phys. Rev. Lett.* **95**, 146802 (2005).
- [85] E. Prodan and H. Schulz-Baldes, Bulk and Boundary Invariants for Complex Topological Insulators (Springer International Publishing Switzerland 2016, 2016).
- [86] W. A. Benalcazar, B. A. Bernevig, and T. L. Hughes, Quantized electric multipole insulators, *Science* **357**, 61 (2017).
- [87] W. A. Benalcazar, B. A. Bernevig, and T. L. Hughes, Electric multipole moments, topological multipole moment pumping, and chiral hinge states in crystalline insulators, *Phys. Rev. B* **96**, 245115 (2017).
- [88] L. C. Venuti and P. Zanardi, Quantum critical scaling of the geometric tensors, *Phys. Rev. Lett.* **99**, 095701 (2007).
- [89] P. Zanardi, P. Giorda, and M. Cozzini, Information-theoretic differential geometry of quantum phase transitions, *Phys. Rev. Lett.* **99**, 100603 (2007).
- [90] A. Carollo, D. Valenti, and B. Spagnolo, Geometry of quantum phase transitions, *Phys. Rept.* **838**, 1 (2020).
- [91] C. Repellin, B. A. Bernevig, and N. Regnault, Z_2 fractional topological insulators in two dimensions, *Phys. Rev. B* **90**,

- 245401 (2014).
- [92] S. H. Simon, F. Harper, and N. Read, Fractional chern insulators in bands with zero berry curvature, *Phys. Rev. B* **92**, 195104 (2015).
- [93] C.-R. Liu, Y.-W. Guo, Z.-J. Li, W. Li, and Y. Chen, Realizing tao-thouless-like state in fractional quantum spin hall effect, *Sci. Rep.* **6**, 33472 (2016).
- [94] Y.-M. Wu, D. Shaffer, Z. Wu, and L. H. Santos, Time-reversal invariant topological moiré flat band: A platform for the fractional quantum spin hall effect, *Phys. Rev. B* **109**, 115111 (2024).
- [95] K. Kang et al., Evidence of the fractional quantum spin hall effect in moiré mote2, *Nature* **628**, 522 (2024).
- [96] K. Kang et al., Time-reversal symmetry breaking fractional quantum spin hall insulator in moiré mote2, *arXiv:2501.02525* (2025).
- [97] Y. Xie et al., *Nature* **600**, 439 (2021).
- [98] Note that the degree of degeneracy factor [52,90] cancels out in the TDI. In this case, the quantum metric, maximal Berry curvature, and 'mirror Berry curvature' are expressed in terms of the many-body wave function with twisted boundary conditions [52,90].
- [99] J. Wang, J. Cano, A. J. Millis, Z. Liu, and B. Yang, Exact landau level description of geometry and interaction in a flatband, *Phys. Rev. Lett.* **127**, 246403 (2021).
- [100] J. Wang, S. Klevtsov, and Z. Liu, Origin of model fractional chern insulators in all topological ideal flatbands: Explicit color-entangled wave function and exact density algebra, *Phys. Rev. Research* **5**, 023167 (2023).
- [101] Z. Z. Alisultanov, Disorder-induced singularity of the quantum metric, *JETP Lett.* **119**, 929 (2024).
- [102] D. N. Basov, R. D. Averitt, D. van der Marel, M. Dressel, and K. Haule, *Rev. Mod. Phys.* **83**, 471 (2011).
- [103] J. Yu, J. Herzog-Arbeitman, and B. A. Bernevig, Universal wilson loop bound of quantum geometry: Z2 bound and physical consequences, *arXiv:2501.00100* (2025).
- [104] W. J. Jankowski, R.-J. Slager, and G. F. Lange, Quantum geometric bounds in spinful systems with trivial band topology, *arXiv:2501.16428* (2025).
- [105] B. A. Bernevig, T. L. Hughes, and S.-C. Zhang, Quantum spin hall effect and topological phase transition in hgte quantum wells, *Science* **314**, 1757 (2006).
- [106] J. Ahn and B.-J. Yang, Unconventional topological phase transition in two-dimensional systems with space-time inversion symmetry, *Phys. Rev. Lett.* **118**, 156401 (2017).
- [107] J. Wang, J. Cano, A. J. Millis, Z. Liu, and B. Yang, Exact landau level description of geometry and interaction in a flatband, *Phys. Rev. Lett.* **127**, 246403 (2021).
- [108] M. Kolodrubetz, V. Gritsev, and A. Polkovnikov, Classifying and measuring geometry of a quantum ground state manifold, *Phys. Rev. B* **88**, 064304 (2013).
- [109] Y.-Q. Ma, S.-J. Gu, S. Chen, H. Fan and W.-M. Liu, The euler number of bloch states manifold and the quantum phases in gapped fermionic systems, *EPL* **103**, 10008 (2013).
- [110] Y.-Q. Ma, Quantum distance and the euler number index of the bloch band in a one-dimensional spin model, *Phys. Rev. E* **90**, 042133 (2014).
- [111] L. Yang, Y.-Q. Ma, and X.-G. Li, Geometric tensor and the topological characterization of the bloch band in a two-band lattice model, *Physica B* **456**, 359 (2015).
- [112] In the calculation of the Gauss curvature, we will encounter the quantum metric having zeros. Fortunately, those zeros are not intrinsic; they only have minimal contributions to the topology and can be moved by topological deformation or simply replaced by a small number, say 0.00000001.
- [113] G. Provost and J. P. Vallee, Riemannian structure on manifolds of quantum states, *Commun. Math. Phys.* **76**, 289 (1980).
- [114] N. Marzari and D. Vanderbilt, Maximally localized generalized wannier functions for composite energy bands, *Phys. Rev. B* **56**, 12847 (1997).
- [115] S. Peotta and P. Törmä, Superfluidity in topologically nontrivial flat bands, *Nat. Commun.* **6**, 8944 (2015).
- [116] J. Herzog-Arbeitman, V. Peri, F. Schindler, S. D. Huber, and B. A. Bernevig, Superfluid weight bounds from symmetry and quantum geometry in flat bands, *Phys. Rev. Lett.* **128**, 087002 (2022).
- [117] J. E. Moore and L. Balents, Topological invariants of time-reversal-invariant band structures, *Phys. Rev. B* **75**, 121306(R) (2007).
- [118] I. Goldbring, A nonstandard proof of the spectral theorem for unbounded self-adjoint operators, *Expositiones Mathematicae* **39**, 590 (2021).
- [119] E. Kreyszig, *Introductory Functional Analysis with Applications* (John Wiley and Sons. Inc., 1978).
- [120] J. E. Avron, R. Seiler, and B. Simon, Homotopy and quantization in condensed matter physics, *Phys. Rev. Lett.* **51**, 51 (1983).
- [121] J. F. Wienand, F. Horn, M. Aidelsburger, J. Bibo, and F. Grusdt, Thouless pumps and bulk-boundary correspondence in higher-order symmetry-protected topological phases, *Phys. Rev. Lett.* **128**, 246602 (2022).
- [122] C.-L. Deng et al., High-order topological pumping on a superconducting quantum processor, *Phys. Rev. Lett.* **133**, 140402 (2024).
- [123] P. D. Lax, *Functional Analysis* (John Wiley and Sons, Inc., 2002).
- [124] N. Verma, T. Hazra, and M. Randeria, Optical spectral weight, phase stiffness and tc bounds for trivial and topological flat band superconductors, *PNAS* **118**, e2106744118 (2021).
- [125] D. Mao and D. Chowdhury, Diamagnetic response and phase stiffness for interacting isolated narrow bands, *PNAS* **120**, e2217816120 (2023).
- [126] J. F. Mendez-Valderrama, D. Mao, and D. Chowdhury, Low-energy optical sum-rule in moiré graphene, *Phys. Rev. Lett.* **133**, 196501 (2024).

End Matter

Appendix A: Factors Influencing the Decay Behavior of Quantum Weight: Crystalline Symmetry, Optical Gap, and Inverse Mass Tensor

Here, we only consider point group symmetry. To begin, we first examine rotational symmetry. As the decay behavior of the quantum weight near the transition from the topological non-trivial to trivial phase is strongly constrained by crystalline symmetries, we classify these crystalline symmetries into three groups, which we denote as \mathcal{S}_1 , \mathcal{S}_2 , and \mathcal{S}_3 : (i) \mathcal{S}_1 contains C_3 and C_6 rotation symmetries, (ii) \mathcal{S}_2 contains C_4 rotation symmetry, and (iii) \mathcal{S}_3 includes crystalline symmetries that lack C_3 , C_4 and C_6 rotation symmetries, as well as other crystalline symmetries with similar representation matrices. For other crystalline symmetries with a similar form of representation matrices for C_3 (i.e., $\begin{pmatrix} a & b \\ c & d \end{pmatrix}$, $a, b, c, d \neq 0$) and C_4 (i.e., $\begin{pmatrix} 0 & \pm 1 \\ \pm 1 & 0 \end{pmatrix}$), they will belong to \mathcal{S}_1 and \mathcal{S}_2 , respectively.

In the following, we will see that the C_3 or C_6 rotation symmetry makes the quantum weight strongly anisotropic, such that $K_{xx} \neq K_{yy}$, where $K_{ab} \equiv 2\pi \int \frac{d^2k}{(2\pi)^2} g_{ab}(\mathbf{k})$. In contrast, symmetries belonging to the group \mathcal{S}_3 have a relatively small effect, with no relation between K_{xx} and K_{yy} . Only the C_4 rotation symmetry can yield $K_{xx} = K_{yy}$. Other composite symmetries with zero diagonal elements and ± 1 off-diagonal elements can also lead to $K_{xx} = K_{yy}$. If $K_{xx} \neq K_{yy}$ or in the presence of C_3 (C_6) rotation symmetry, the decay of the quantum weight near the transition from the topological non-trivial to trivial phase is slow, making the optical conductivity difficult to use for identifying the topology. Fortunately, a larger optical gap E_g (and/or effective mass) [36, 79] (see Fig. 3) or flattening the band can cause K_{xx} and K_{yy} to decay rapidly.

To see how rotation symmetry provides a connection between elements of the quantum metric (matrix), let R and \mathcal{R} be point-group symmetry operations in real (momentum) and orbital bases, respectively: $x'_a = \sum_b R_{ab} x_b$ and $k'_a = \sum_b R_{ab}^{-1} k_b$. Additionally, $H'(\mathbf{k}) = \mathcal{R}H(\mathbf{k}')\mathcal{R}^{-1}$ and $|u'_n(\mathbf{k})\rangle = \mathcal{R}|u_n(\mathbf{k}')\rangle$. Hence, the transformation of the quantum metric [55] can be written as

$$g_{ba}(\mathbf{k}) = \sum_{b'a'} R_{bb'} R_{aa'} g_{b'a'}(\mathbf{k}'). \quad (\text{A1})$$

When substituting $C_3 = \begin{pmatrix} -1/2 & -\sqrt{3}/2 \\ \sqrt{3}/2 & -1/2 \end{pmatrix}$ into Eq. (A1), we obtain $g_{xx}(\mathbf{k}) = \frac{1}{4}g_{xx}(\mathbf{k}') + \frac{\sqrt{3}}{4}g_{xy}(\mathbf{k}') + \frac{\sqrt{3}}{4}g_{yx}(\mathbf{k}') + \frac{3}{4}g_{yy}(\mathbf{k}')$. Obviously, $g_{xx}(\mathbf{k}) \neq g_{yy}(\mathbf{k}')$ unless $g_{ba}(\mathbf{k}') = 0$. However, the $C_4 = \begin{pmatrix} 0 & -1 \\ 1 & 0 \end{pmatrix}$ rotation symmetry can enforce $g_{xx}(\mathbf{k}) = g_{yy}(\mathbf{k}')$, which reduces the anisotropy of quantum geometry and lowers the "geometric effect", as we will discuss below. As a result, we obtain $K_{xx} = K_{yy}$ for systems preserving C_4 rotation symmetry. The condition of

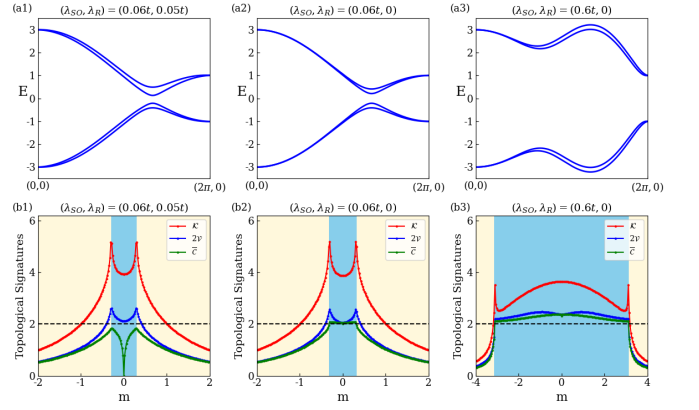


FIG. 3. Band structure and topological signatures of the Kane-Mele model with three sets of $(\lambda_{SO}, \lambda_R)$ parameters. (a1-a3) Band structure with (a1) $(\lambda_{SO}, \lambda_R) = (0.06t, 0.05t)$, (a2) $(\lambda_{SO}, \lambda_R) = (0.06t, 0)$, and (a3) $(\lambda_{SO}, \lambda_R) = (0.6t, 0)$, in which we set $\lambda_v = 0.1t$. (b1-b3) The topological signatures \mathcal{K} , $2\mathcal{V}$ and $\overline{\mathcal{C}}$ with (b1) $(\lambda_{SO}, \lambda_R) = (0.06t, 0.05t)$, (b2) $(\lambda_{SO}, \lambda_R) = (0.06t, 0)$, and (b3) $(\lambda_{SO}, \lambda_R) = (0.6t, 0)$ as a function of m . The black dashed line represents the number of boundary states. Here we set $t = 1$. The presence of Rashba spin-orbit coupling, which breaks the mirror symmetry (M_z), will lower the value of MBC.

$K_{xx} = K_{yy}$ is important for the rapid decay of the quantum weight near the transition from the topological nontrivial to trivial phase. In addition to C_4 rotation symmetry, the magnitude of the band-inversion parameter is also a key factor influencing the rapid decay of the quantum weight in certain cases (for example, spin-orbit coupling should be smaller than the nearest neighbor hopping in the Bernevig-Hughes-Zhang model [105, 106]).

Another factor that influences the decay behavior of quantum weight is the optical gap (E_g) [36] and the inverse mass tensor in the "topological" inequality [36, 79]: $\frac{\pi e^2}{2} \frac{\mathcal{M}}{E_g} \geq \mathcal{K} \geq 2\mathcal{V} \geq \overline{\mathcal{C}} \geq \sum_{s=1}^{sec} |\mathcal{N}_s|$, where $\mathcal{M} = \sum_{m,n,a} \int \frac{d\mathbf{k}}{(2\pi)^2} [M_{mn}^{-1}(\mathbf{k})]_{aa} \langle c_{\mathbf{k}m}^\dagger c_{\mathbf{k}n} \rangle$ and $[M_{mn}^{-1}(\mathbf{k})]_{aa} = \sum_{\alpha\beta} U_{m,\alpha}^\dagger \frac{\partial^2 H_{\alpha\beta}(\mathbf{k})}{\partial(\hbar k_a)^2} U_{\beta,n}(\mathbf{k})$ is the inverse mass tensor [49, 80]. A larger value of E_g can bring \mathcal{K} , $2\mathcal{V}$ and $\overline{\mathcal{C}}$ closer together. For example, in the Kane-Mele model, we can obtain a sufficiently large E_g by setting a larger λ_{SO} , say $0.6t$ (see Fig. 3(b3)). The non-vanishing of quantum weight in the trivial phase can be interpreted as the "geometric effect", which is related to the inverse mass tensor. Therefore, flattening the band can also enhance the decay of the quantum weight in the trivial phase.

The condition for obtaining quantized quantum volume is subtle. Here, we list two classes of possible conditions: (i) the system preserves C_4 symmetry and has even-function matrix elements in the Hamiltonian, such as the TCI model of mirror-protected insulator [61]; and (ii) the system has ideal flat bands [82, 107].

Appendix B: Euler Number and Its Relation to Chern Number

Unlike the Chern number, which is expressed in terms of the Berry curvature, the Euler number is expressed in terms of the Gauss curvature in the context of Riemannian geometry [56, 77, 108–111]. However, their exact relationship is still unclear.

Here, we follow the approach of Ahn et al. [56] to provide the formula for the Gauss curvature and its associated Gauss-Bonnet theorem. It is well-known that the 2D Gauss-Bonnet theorem connects the Euler characteristic to the integrand of the Gauss curvature [77]:

$$\chi = \frac{1}{2\pi} \int K d\mathbf{A}, \quad (\text{B1})$$

where $K = R_{xyxy}(\mathbf{k}) / \det g(\mathbf{k})$ and $d\mathbf{A} = \sqrt{\det g(\mathbf{k})} dk_x \wedge dk_y$ are the Gauss curvature and the oriented area element [77], respectively. By a similar derivation in Ref. [56], we can obtain the expression for the non-Abelian Riemannian curvature tensor as follows:

$$R_{badc}(\mathbf{k}) = \frac{1}{2} \text{tr}(\hat{\Omega}_{ba}^{occ} \hat{\Omega}_{dc}^{occ}), \quad (\text{B2})$$

where $\hat{\Omega}_{ba}^{occ}$ is the matrix of non-Abelian Berry curvature for the occupied band, and its corresponding matrix element is $\Omega_{ba}^{n_1 n_2} = -2\Im(\sum_{m \in unocc} r_{n_1 m}^b r_{m n_2}^a)$ [55, 56]. Similarly, the Abelian Riemannian curvature tensor is given by

$$R_{badc}^n(\mathbf{k}) = \frac{1}{2} \Omega_{ba}^n \Omega_{dc}^n, \quad (\text{B3})$$

where $\Omega_{ba}^n = -2\Im(\sum_{m \neq n} r_{nm}^b r_{mn}^a)$. Both the Abelian and non-Abelian Riemannian curvature tensors satisfy three algebraic relations [77]: (i) $R_{badc}(\mathbf{k}) = R_{dcba}(\mathbf{k})$, (ii) $R_{badc}(\mathbf{k}) = -R_{abdc}(\mathbf{k}) = -R_{bacd}(\mathbf{k})$, (iii) $R_{badc}(\mathbf{k}) + R_{bdca}(\mathbf{k}) + R_{bcad}(\mathbf{k}) = 0$. In 2D, only the components R_{bababa} are nonzero. The Euler number we define is slightly different from that in Ref. [56], where the Riemannian curvature tensor is defined in a two-level setting. In our approach, we define the Riemannian curvature tensor for both occupied bands and any separable single band, which can reduce to the Chern number when the band is ideal flat [82, 107], as we discuss below.

There should be some possible approaches to obtain an integer Euler number. One such approach is for the quantum state manifold to have constant Gauss curvature and quantum volume. In this case, the Gauss-Bonnet theorem can be simplified to $\chi = K\mathcal{V}$ [78]. We can see that when (i) both K and \mathcal{V} are integers, or (ii) K and \mathcal{V} are not integers but their product is an integer, the Euler number is topological. In the case of the TCI model of a mirror-protected insulator [61], we have $K = 1$ [112] and $\mathcal{V} = 2$. As a result, the Euler number of the TCI model is equal to 2 (see Fig. 4(b)). In the Kane-Mele model and the HOTI model, both K and \mathcal{V} are not integers. Thus, their Euler numbers are not quantized (see Fig. 4(a,c)).

To reveal the relationship between the Euler number and the Chern number, we rewrite the Gauss-Bonnet theorem for

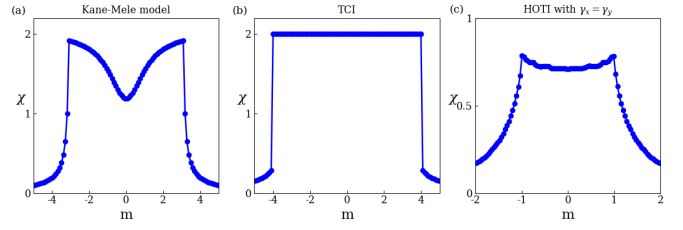


FIG. 4. Euler numbers of the Kane-Mele model, the TCI model of mirror-protected insulator, and the HOTI model of quadrupole insulator as functions of m . (a) Euler number of the Kane-Mele model with $(t, \lambda_{SO}, \lambda_R, \lambda_v) = (1, 0.6t, 0, m)$. (b) Euler number of the TCI model of mirror-protected insulator with $(t_1, t_2, t_{PH}, v_s, v_m) = (2, 1.5, 0.1, 1.3, m)$. (c) Euler number of the HOTI model of quadrupole insulator with $(\lambda_x, \lambda_y, \gamma_x, \gamma_y) = (1, 1, m, m)$.

a single band in the following form:

$$\chi_n = \frac{1}{2\pi} \int \frac{R_{xyxy}^n(\mathbf{k})}{\det g^n(\mathbf{k})} d\mathbf{A}, \quad (\text{B4})$$

where $d\mathbf{A} = \text{sgn}(\Omega_{xy}(\mathbf{k})) \sqrt{\det g^n(\mathbf{k})} dk_x dk_y$ is the oriented area element [56, 77]. Substituting $R_{xyxy}^n(\mathbf{k}) = \frac{1}{2} \Omega_{xy}^n(\mathbf{k}) \Omega_{xy}^n(\mathbf{k})$ into Eq. (B4), we obtain

$$\chi_n = \frac{1}{2\pi} \int \frac{|\Omega_{xy}^n(\mathbf{k})|^2 \Omega_{xy}^n(\mathbf{k})}{2\sqrt{\det g^n(\mathbf{k})}} dk_x dk_y. \quad (\text{B5})$$

When the band is ideal flat [82, 107], i.e., when the relation $2\sqrt{\det g^n(\mathbf{k})} = |\Omega_{dc}^n(\mathbf{k})|$ holds, we finally obtain:

$$\chi_n = \frac{1}{2\pi} \int \Omega_{xy}^n(\mathbf{k}) dk_x dk_y = C_n. \quad (\text{B6})$$

The Eq. (B5) explains why the Euler number is not zero in a topologically trivial phase: the relation $2\sqrt{\det g^n(\mathbf{k})} > |\Omega_{xy}^n(\mathbf{k})|$ holds for dispersive bands. However, we always have $2\sqrt{\det g^n(\mathbf{k})} = |\Omega_{xy}^n(\mathbf{k})|$ in the two-band systems [69]. In the case of multiple bands, we can also reduce the Euler number to the Chern number if certain conditions are satisfied. To demonstrate this, we can diagonalize the matrix $\hat{\Omega}_{xy}^{occ}$. Thus, the Riemannian curvature tensor can be rewritten as $R_{xyxy}(\mathbf{k}) = \frac{1}{2} \sum_{n \in occ} F_{xy}^n(\mathbf{k}) F_{xy}^n(\mathbf{k})$, where $F_{xy}^n(\mathbf{k})$ is the eigenvalue of $\hat{\Omega}_{xy}^{occ}$. If we allow each band to have its own orientation and be ideal flat i.e., $2\sqrt{\det g(\mathbf{k})} = |F_{xy}^n(\mathbf{k})|$, we can also obtain $\chi_n = C_n$ for each occupied band. However, the total Euler number of the occupied bands will be $\sum_{n \in occ} |\chi_n|$. Note that Euler number can apply to both TRS and broken TRS, as long as the bands are ideal flat or exhibit quantized Gauss curvature and quantum volume.

Supplemental Material: Topological Signatures of the Optical Bound on Maximal Berry Curvature: Application to Two-Dimensional Time-Reversal-Symmetric Insulators

In this supplementary material, we review several aspects of quantum geometry and provide a detailed derivation of the refined TDI, the optical bound, the SWM sum rule, and the relationship between the optical bound and quantum weight. Finally, we present additional numerical results to enhance the understanding of the main concepts.

1: Quantum geometry of occupied bands

In this section, we review some basic concepts of quantum geometry. We follow the approach recently introduced by Ahn et al. [S55, S56], who utilize an analogous definition from differential geometry [S77] to derive the quantum metric tensor and Berry curvature, which are equivalent to the conventional approach [S113, S114]. A key step in their method involves defining the tangent vector basis and the associated inner product for quantum states, which can be treated as a manifold. In the context of optical transitions between states m and n with $m \neq n$, one can choose the tangent vector as follows:

$$\hat{e}_a^{mn}(\mathbf{k}) \equiv r_{mn}^a(\mathbf{k})|u_m(\mathbf{k})\rangle\langle u_n(\mathbf{k})|, \quad a = 1, \dots, d. \quad (\text{S1})$$

where the interband Berry connection is given by $r_{mn}^a(\mathbf{k}) = i\langle u_m(\mathbf{k})|\partial_a|u_n(\mathbf{k})\rangle$. For the complex Riemannian structure, one can use the Hilbert-Schmidt inner product:

$$(A, B) = \sum_{m,n} A_{mn}^* B_{mn} = \text{tr}(A^\dagger B). \quad (\text{S2})$$

From the two definitions above, we can obtain the Hermitian metric tensor for any pair of bands,

$$Q_{ba}^{mn}(\mathbf{k}) \equiv (\hat{e}_b^{mn}(\mathbf{k}), \hat{e}_a^{mn}(\mathbf{k})) = r_{nm}^b(\mathbf{k})r_{mn}^a(\mathbf{k}). \quad (\text{S3})$$

This interband-resolved geometric quantity, $Q_{ba}^{mn}(\mathbf{k}) = g_{ba}^{mn}(\mathbf{k}) - i\Omega_{ba}^{mn}/2(\mathbf{k})$ is the component of quantum geometric tensor [S114] in multiband case. Note that there is no band summation. $Q_{ba}^{mn}(\mathbf{k})$ itself can be understood as the quantum geometric tensor for manifold of two-band subspace. For the occupied bands case, one can generalize $\hat{e}_a^{mn}(\mathbf{k})$ to

$$\hat{e}_a(\mathbf{k}) \equiv \sum_{n \in \text{occ}} \sum_{m \in \text{unocc}} |u_m(\mathbf{k})\rangle r_{mn}^a(\mathbf{k}) \langle u_n(\mathbf{k})|, \quad (\text{S4})$$

as the tangent vector in complex Grassmannian manifold of occupied bands [S56]. Hence we obtain the quantum geometric tensor of the occupied bands:

$$Q_{ba}(\mathbf{k}) \equiv (\hat{e}_b(\mathbf{k}), \hat{e}_a(\mathbf{k})) = \sum_{n \in \text{occ}} \sum_{m \in \text{unocc}} r_{nm}^b(\mathbf{k})r_{mn}^a(\mathbf{k}). \quad (\text{S5})$$

Further, the quantum geometric tensor of the occupied bands can be expressed as [S55],

$$Q_{ab}(\mathbf{k}) = \sum_{n \in \text{occ}} \sum_{m \in \text{unocc}} r_{nm}^a(\mathbf{k})r_{mn}^b(\mathbf{k}) = \sum_{n \in \text{occ}} (g_{ab}^{nn}(\mathbf{k}) - \frac{i}{2}\Omega_{ab}^{nn}(\mathbf{k})) = g_{ab}(\mathbf{k}) - \frac{i}{2}\Omega_{ab}(\mathbf{k}), \quad (\text{S6})$$

where the non-Abelian quantum metric and non-Abelian Berry curvature are

$$\begin{aligned} Q_{ab}(\mathbf{k}) &= \sum_{n \in \text{occ}} \sum_{m \in \text{unocc}} \langle \partial_a u_n(\mathbf{k}) | u_m(\mathbf{k}) \rangle \langle u_m(\mathbf{k}) | \partial_b | u_n(\mathbf{k}) \rangle \\ &= \sum_{n \in \text{occ}} \langle \partial_a u_n(\mathbf{k}) | (1 - P(\mathbf{k})) | \partial_b u_n(\mathbf{k}) \rangle \\ &= \sum_{n \in \text{occ}} [g_{ab}^{n,n}(\mathbf{k}) - \frac{i}{2}\Omega_{ab}^{nn}(\mathbf{k})], \end{aligned} \quad (\text{S7})$$

Here we use a relation [S56]

$$\begin{aligned} \sum_{m \in \text{unocc}} r_{n_1 m}^a(\mathbf{k}) r_{m n_2}^b(\mathbf{k}) &= \sum_{m \in \text{unocc}} \langle \partial_a u_{n_1}(\mathbf{k}) | u_m(\mathbf{k}) \rangle \langle u_m(\mathbf{k}) | \partial_b | u_{n_2}(\mathbf{k}) \rangle \\ &= \langle \partial_a u_{n_1}(\mathbf{k}) | (1 - P(\mathbf{k})) | \partial_b u_{n_2}(\mathbf{k}) \rangle \\ &= g_{ab}^{n_1 n_2}(\mathbf{k}) - \frac{i}{2}\Omega_{ab}^{n_1 n_2}(\mathbf{k}), \end{aligned} \quad (\text{S8})$$

where the projection operator is give by $P(\mathbf{k}) = \sum_{n \in occ} |u_n(\mathbf{k})\rangle\langle u_n(\mathbf{k})|$.

One also can express the quantum geometric tensor using the projection operator [S115, S116], with a form $P(\mathbf{k}) = U(\mathbf{k})U^\dagger(\mathbf{k})$, where $U(\mathbf{k})$ is the $N \times N_{occ}$ matrix whose columns are the eigenvectors of the occupied bands. Here N is the number of band. Similarly, one can define a tangent vector, which is a covariant derivative acting on $U(\mathbf{k})$, i.e., $(1 - U(\mathbf{k})U^\dagger(\mathbf{k}))\partial_a U(\mathbf{k})$. Using the Hilbert-Schmidt inner product again, the quantum geometric tensor can be defined as

$$Q_{ab}(\mathbf{k}) = \text{tr}(((1 - U(\mathbf{k})U^\dagger(\mathbf{k}))\partial_a U(\mathbf{k}))^\dagger(1 - U(\mathbf{k})U^\dagger(\mathbf{k}))\partial_b U(\mathbf{k})). \quad (\text{S9})$$

After some algebra (see Ref. [S116]), we obtain:

$$Q_{ab}(\mathbf{k}) = \text{tr}(P(\mathbf{k})\partial_a P(\mathbf{k})\partial_b P(\mathbf{k})) = g_{ab}(\mathbf{k}) - \frac{i}{2}\Omega_{ab}(\mathbf{k}), \quad (\text{S10})$$

where the non-Abelian quantum metric and non-Abelian Berry curvature are

$$g_{ab}(\mathbf{k}) = \frac{1}{2}\text{tr}(\partial_a P(\mathbf{k})\partial_b P(\mathbf{k})), \quad \Omega_{ab}(\mathbf{k}) = i\text{tr}(P(\mathbf{k})[\partial_a P(\mathbf{k}), \partial_b P(\mathbf{k})]). \quad (\text{S11})$$

2. Trace-determinant inequality and its refinement for TIs, TCIs, and HOTIs with a topological lower bound

In this subsection, we will prove the TDI and its refinement for TIs/TCIs and HOTIs using the spin projection operator and Wannier bases, respectively. As enforced by time-reversal symmetry, we know that the Chern number of the occupied bands is zero in the usual basis [S117]. However, when projecting the occupied bands onto different spin (pseudospin) or topological sectors, i.e., replacing $P(\mathbf{k}) = \sum_{n=1}^{occ} |u_n(\mathbf{k})\rangle\langle u_n(\mathbf{k})|$ by $P(\mathbf{k})\hat{s}P(\mathbf{k})$, we can obtain nonzero Chern number in a TRS system, where s is the (pseudo) spin operator. Crucially, the choice of \hat{s} is subject to the following two constraints [S71, S76]:

$$P(\mathbf{k})|\psi_i(\mathbf{k})\rangle = |\psi_i(\mathbf{k})\rangle, \quad (\text{S12})$$

$$P(\mathbf{k})\hat{s}P(\mathbf{k})|\psi_i(\mathbf{k})\rangle = \lambda_i|\psi_i(\mathbf{k})\rangle. \quad (\text{S13})$$

We can view both $P(\mathbf{k})$ and $P(\mathbf{k})\hat{s}P(\mathbf{k})$ as flattening Hamiltonians. From the spectral theorem [S118] and the spectral representation [S119], we can re-express $P(\mathbf{k})$ using the eigenvalues ($\lambda_i = 0, \lambda_\pm$) and eigenstates ($|\psi_i^\pm(\mathbf{k})\rangle$) of $P(\mathbf{k})\hat{s}P(\mathbf{k})$, i.e., $P(\mathbf{k}) = \lambda_+ \sum_{i=1}^{N_+} |\psi_i^+(\mathbf{k})\rangle\langle\psi_i^+(\mathbf{k})| + \lambda_- \sum_{i=1}^{N_-} |\psi_i^-(\mathbf{k})\rangle\langle\psi_i^-(\mathbf{k})|$. As a result, we obtain $P(\mathbf{k}) = \lambda_+ \sum_{i=1}^{N_+} |\psi_i^+(\mathbf{k})\rangle\langle\psi_i^+(\mathbf{k})| + \lambda_- \sum_{i=1}^{N_-} |\psi_i^-(\mathbf{k})\rangle\langle\psi_i^-(\mathbf{k})| = \sum_{n=1}^{occ} |u_n(\mathbf{k})\rangle\langle u_n(\mathbf{k})|$. In other words, $P(\mathbf{k})$ has two different sets of eigenstates $\{|\psi_i^\pm(\mathbf{k})\rangle\}$ and $\{|u_n(\mathbf{k})\rangle\}$, which represent the same system. In fact, $|\psi_i^\pm(\mathbf{k})\rangle$ is simply a linear combination of $|u_n(\mathbf{k})\rangle$.

For the Kane-Mele model and TCI, we choose $\hat{s} = \tau_0\sigma_z$, where τ_0 is the two-dimensional identity matrix. Note that the choice of the spin operator should match the basis of the Hamiltonian. As pointed out in Ref. [S76], only the lowest and topmost spin-resolved bands are physically relevant. We denote the projection of the spin-resolved band as $P_\pm(\mathbf{k}) = |\psi^\pm(\mathbf{k})\rangle\langle\psi^\pm(\mathbf{k})|$. Using these two spin-resolved band projections, we obtain the corresponding non-Abelian quantum metric and non-Abelian Berry curvature:

$$g'_{ab}(\mathbf{k}) = \frac{1}{2}\text{tr}(\partial_a P'(\mathbf{k})\partial_b P'(\mathbf{k})), \quad \Omega'_{ab}(\mathbf{k}) = i\text{tr}(P'(\mathbf{k})[\partial_a P'(\mathbf{k}), \partial_b P'(\mathbf{k})]), \quad (\text{S14})$$

where $P'(\mathbf{k}) = P_+(\mathbf{k}) + P_-(\mathbf{k})$. Obviously, we have $g'_{ab}(\mathbf{k}) = g_{ab}(\mathbf{k})$ since $|\psi_i^\pm(\mathbf{k})\rangle$ and $|u_n(\mathbf{k})\rangle$ represent the same projection operator. A crucial part of proving the refined TDI and obtaining the topological lower bound is the general inequality: $2\sqrt{\det \overline{g}(\mathbf{k})} \geq \overline{\Omega}_{ab}(\mathbf{k})$, which we have proved below. On the other hand, by the sum rule of the Berry curvature or Chern number [S120], we have $\Omega'_{ab}(\mathbf{k}) = \Omega_{ab}^+(\mathbf{k}) + \Omega_{ab}^-(\mathbf{k})$. Hence, it follows that $\overline{\Omega}'_{ab}(\mathbf{k}) \geq |\Omega_{ab}^+(\mathbf{k})| + |\Omega_{ab}^-(\mathbf{k})| \geq \Omega'_{ab}(\mathbf{k})$. Finally, we obtain the TDI for TIs and TCIs:

$$g'_{xx}(\mathbf{k}) + g'_{yy}(\mathbf{k}) \geq 2\sqrt{\det g'(\mathbf{k})} \geq \overline{\Omega}'_{ab}(\mathbf{k}) \geq |\Omega_{ab}^+(\mathbf{k})| + |\Omega_{ab}^-(\mathbf{k})|. \quad (\text{S15})$$

In other words, the quantum metric is the same in different bases, but the topology only manifests in certain bases. After integrating over the momentum variable in the first Brillouin zone, we obtain the refined inequality for TIs and TCIs with a topological lower bound:

$$\int \frac{d^2\mathbf{k}}{2\pi} (g'_{xx}(\mathbf{k}) + g'_{yy}(\mathbf{k})) \geq \int \frac{d^2\mathbf{k}}{2\pi} (2\sqrt{\det g'(\mathbf{k})}) \geq \int \frac{d^2\mathbf{k}}{2\pi} \overline{\Omega}'_{ab}(\mathbf{k}) \geq \left| \int \frac{d^2\mathbf{k}}{2\pi} \Omega_{ab}^+(\mathbf{k}) \right| + \left| \int \frac{d^2\mathbf{k}}{2\pi} \Omega_{ab}^-(\mathbf{k}) \right|, \quad (\text{S16})$$

where we use the fact that $\int \frac{d^2\mathbf{k}}{2\pi} |\Omega_{ab}^\pm(\mathbf{k})| \geq \left| \int \frac{d^2\mathbf{k}}{2\pi} \Omega_{ab}^\pm(\mathbf{k}) \right|$. We label it as $\mathcal{K}' \geq 2\mathcal{V}' \geq \overline{C}' \geq |C_+| + |C_-|$, where \mathcal{K}' , \mathcal{V}' , \overline{C}' , and C_\pm are the quantum weight, quantum volume, "pseudo-Chern number", and spin Chern number of the spin-resolved bands, respectively.

Next, we prove the refined TDI for HOTIs. Since the original eigenvalues of the Wilson loop, where $\mathcal{W}_{x,k_y} |\nu_{x,k_y}^j\rangle = e^{i2\pi\nu_x^j(k_y)} |\nu_{x,k_y}^j\rangle$ and $j = 1, \dots, N_{occ}$, cannot identify the topology of HOTIs, a projection method [S76] or basis transformation was used [S86]. Following the work of Ref. [S86], we define the Wannier band basis as

$$|w_{x,k_y}^j\rangle = \sum_{n=1}^{N_{occ}} |u_n(\mathbf{k})\rangle [\nu_{x,k_y}^j]^n, \quad (\text{S17})$$

where $[\nu_{x,k_y}^j]^n$ is the components of the eigenvectors $|\nu_{x,k_y}^j\rangle$. We observe that the Wannier band basis can be obtained using the projection operator method as described in Ref. [S76]. For simplicity, we consider only the case of two occupied bands. Unlike previous work [S86], we take into account both Wannier sectors ν_x^+ and ν_x^- . Now the reduced spin matrix $\langle u_m(\mathbf{k}) | \hat{s} | u_n(\mathbf{k}) \rangle$ and its eigenvectors [S76] are now replaced by the Wilson loop \mathcal{W}_{x,k_y} and its eigenvectors, respectively. As a result, the corresponding projection operator for HOTIs can be constructed as $P(\mathbf{k}) \hat{w}_{x,k_y} P(\mathbf{k})$, where $\hat{w}_{x,k_y} = \tau_0 \otimes \mathcal{W}_{x,k_y}$. Therefore, their quantum metrics, quantum weight, and volumes are the same, i.e., $\tilde{g}_{ab}(\mathbf{k}) = g_{ab}(\mathbf{k})$, $\tilde{\mathcal{K}} = \int \frac{d^2\mathbf{k}}{2\pi} (\tilde{g}_{xx}(\mathbf{k}) + \tilde{g}_{yy}(\mathbf{k})) = \mathcal{K}$, and $\tilde{\mathcal{V}} = \int \frac{d^2\mathbf{k}}{2\pi} (2\sqrt{\det g'(\mathbf{k})}) = \mathcal{V}$, where $\tilde{g}_{ab}(\mathbf{k}) = \frac{1}{2} \text{tr}(\partial_a \tilde{P}(\mathbf{k}) \partial_b \tilde{P}(\mathbf{k}))$ and $\tilde{P}(\mathbf{k}) = |w_{x,k_y}^+\rangle \langle w_{x,k_y}^+| + |w_{x,k_y}^-\rangle \langle w_{x,k_y}^-|$. Similarly, we can define the Berry curvature of the Wannier band as $\tilde{\Omega}_{ab}(\mathbf{k}) = i \text{tr}(\tilde{P}(\mathbf{k}) [\partial_a \tilde{P}(\mathbf{k}), \partial_b \tilde{P}(\mathbf{k})]) = \tilde{\Omega}_{ab}^+(\mathbf{k}) + \tilde{\Omega}_{ab}^-(\mathbf{k})$ [S120]. For the Wannier bases, one can define the corresponding Chern number [S86, S87]:

$$\tilde{C}_\pm = \Delta q_{xy}^\pm / e = \int_0^{2\pi} d\tau \partial_\tau p_l^{\nu_i^\pm}(\tau) = 1, \quad (\text{S18})$$

for $i, l = x, y$ and $i \neq l$, where the polarization over the Wannier sectors ν_x^\pm is

$$p_l^{\nu_i^\pm}(\tau) = -\frac{i}{2\pi} \log \det[\tilde{\mathcal{W}}_{l,\tau}^{\nu_i}], \quad (\text{S19})$$

and the Wilson loop is

$$[\tilde{\mathcal{W}}_{l,\tau}^{\nu_i}]^{jj'} = \langle w_{i,\tau+N_\tau\Delta_\tau}^j | w_{i,\tau+(N_\tau-1)\Delta_\tau}^j \rangle \langle w_{i,\tau+(N_\tau-1)\Delta_\tau}^j | \dots | w_{i,\tau+\Delta_\tau}^j \rangle \langle w_{i,\tau+\Delta_\tau}^j | w_{i,\tau}^{j'} \rangle. \quad (\text{S20})$$

The essence of the above Chern number corresponds to quantized dipole pumping [S86, S87, S121, S122]. Again, using the general inequality $2\sqrt{\det g(\mathbf{k})} \geq \overline{\Omega}_{ab}(\mathbf{k})$ and the fact that $\int \frac{d^2\mathbf{k}}{2\pi} |\tilde{\Omega}_{ab}^\pm(\mathbf{k})| \geq \left| \int \frac{d^2\mathbf{k}}{2\pi} \tilde{\Omega}_{ab}^\pm(\mathbf{k}) \right|$, we obtain the TDI of HOTIs: $\tilde{\mathcal{K}} \geq 2\tilde{\mathcal{V}} \geq \overline{C} \geq |\tilde{C}_+| + |\tilde{C}_-|$, where \overline{C} is the "pseudo-Chern number" of Wannier band. Due to the specific structure of dipole pumping, one also can use the polarization over the Wannier sectors to characterize the topology of HOTIs, i.e., the overall topology of occupied bands can be expressed as $(p_y^{\nu_x^\pm}, p_x^{\nu_y^\pm}) = (1/2, 1/2)$. Therefore, we have $p_y^{\nu_x^+} + p_x^{\nu_y^+} + p_y^{\nu_x^-} + p_x^{\nu_y^-} = |\tilde{C}_+| + |\tilde{C}_-|$.

Finally, we will prove the crucial part of the refined TDI: $2\sqrt{\det(g(\mathbf{k}))} \geq \overline{\Omega}_{ab}(\mathbf{k})$. Using the Cauchy-Schwarz inequality [S123]: $\langle \mathbf{u} | \mathbf{u} \rangle \langle \mathbf{v} | \mathbf{v} \rangle \geq |\langle \mathbf{u} | \mathbf{v} \rangle|^2$, and substituting $\mathbf{u} = |u_m(\mathbf{k})\rangle r_{mn}^a(\mathbf{k}) \langle u_n(\mathbf{k})|$ and $\mathbf{v} = |u_m(\mathbf{k})\rangle r_{mn}^b(\mathbf{k}) \langle u_n(\mathbf{k})|$ into it, we have $g_{aa}^{mn}(\mathbf{k}) g_{bb}^{mn}(\mathbf{k}) \geq (g_{ab}^{mn}(\mathbf{k}))^2 + (\Omega_{ab}^{mn}(\mathbf{k})/2)^2$. By moving $(g_{ab}^{mn}(\mathbf{k}))^2$ to the left-hand side, taking the square root, and performing the band summation, we obtain

$$\sum_{n \in occ} \sum_{m \in unocc} \sqrt{g_{aa}^{mn}(\mathbf{k}) g_{bb}^{mn}(\mathbf{k}) - (g_{ab}^{mn}(\mathbf{k}))^2} \geq \frac{1}{2} \sum_{n \in occ} \sum_{m \in unocc} |\Omega_{ab}^{mn}(\mathbf{k})|. \quad (\text{S21})$$

On the other hand, we have

$$\begin{aligned}
& \sum_{n \in \text{occ}} \sum_{m \in \text{unocc}} \sqrt{g_{aa}^{mn}(\mathbf{k})g_{bb}^{mn}(\mathbf{k}) - (g_{ab}^{mn}(\mathbf{k}))^2} \\
&= \sum_{n \in \text{occ}} \sum_{m \in \text{unocc}} \sqrt{\left(\sqrt{g_{aa}^{mn}(\mathbf{k})g_{bb}^{mn}(\mathbf{k})} - g_{ab}^{mn}(\mathbf{k})\right) \left(\sqrt{g_{aa}^{mn}(\mathbf{k})g_{bb}^{mn}(\mathbf{k})} + g_{ab}^{mn}(\mathbf{k})\right)} \\
&\leq \sqrt{\sum_{n \in \text{occ}} \sum_{m \in \text{unocc}} \left(\sqrt{g_{aa}^{mn}(\mathbf{k})g_{bb}^{mn}(\mathbf{k})} - g_{ab}^{mn}(\mathbf{k})\right)} \sqrt{\sum_{n \in \text{occ}} \sum_{m \in \text{unocc}} \left(\sqrt{g_{aa}^{mn}(\mathbf{k})g_{bb}^{mn}(\mathbf{k})} + g_{ab}^{mn}(\mathbf{k})\right)} \\
&= \sqrt{\left(\sum_{n \in \text{occ}} \sum_{m \in \text{unocc}} \sqrt{g_{aa}^{mn}(\mathbf{k})g_{bb}^{mn}(\mathbf{k})}\right)^2 - \left(\sum_{n \in \text{occ}} \sum_{m \in \text{unocc}} g_{ab}^{mn}(\mathbf{k})\right)^2} \\
&\leq \sqrt{\left(\sum_{n \in \text{occ}} \sum_{m \in \text{unocc}} g_{aa}^{mn}(\mathbf{k})\right) \left(\sum_{n \in \text{occ}} \sum_{m \in \text{unocc}} g_{bb}^{mn}(\mathbf{k})\right) - \left(\sum_{n \in \text{occ}} \sum_{m \in \text{unocc}} g_{ab}^{mn}(\mathbf{k})\right)^2} \\
&= \sqrt{\det g(\mathbf{k})}. \tag{S22}
\end{aligned}$$

In the above derivation, we use the summation form of the Cauchy-Schwarz inequality for the two inequality symbols [S69]. Therefore, we obtain the desired inequality $2\sqrt{\det g(\mathbf{k})} \geq \bar{\Omega}_{xy}(\mathbf{k})$. Obviously, we have $\bar{\Omega}_{xy}(\mathbf{k}) \geq |\Omega_{xy}(\mathbf{k})|$.

3: Optical bound

In this subsection, we derive the optical bound from the refined TDI. Firstly, we explicitly write down the expressions for the non-Abelian quantum metric and the non-Abelian MBC.

$$g_{ab}(\mathbf{k}) = \sum_{m \in \text{occ}} \sum_{n \in \text{unocc}} \Re(r_{mn}^a(\mathbf{k})r_{nm}^b(\mathbf{k})), \tag{S23}$$

$$\bar{\Omega}_{ab}(\mathbf{k}) = \sum_{m \in \text{occ}} \sum_{n \in \text{unocc}} |-2\Im(r_{mn}^a(\mathbf{k})r_{nm}^b(\mathbf{k}))|. \tag{S24}$$

Then the refined TDI becomes

$$\sum_{m \in \text{occ}} \sum_{n \in \text{unocc}} \Re(r_{mn}^x r_{nm}^x + r_{mn}^y r_{nm}^y) - \sum_{m \in \text{occ}} \sum_{n \in \text{unocc}} |-2\Im(r_{mn}^x r_{nm}^y)| \geq 0. \tag{S25}$$

Here, we neglect the term $2\sqrt{\det g(\mathbf{k})}$. Using the identities $r_{mn}^a = \hbar v_{mn}^a / (iE_{mn})$, and $|v_{mn}^x \pm i v_{mn}^y|^2 = |v_{mn}^x|^2 + |v_{mn}^y|^2 \mp i(v_{mn}^x v_{nm}^y - v_{mn}^y v_{nm}^x)$ which is always semi-positive [S83], the refined TDI then reduces to the following form:

$$\sum_{m \in \text{occ}} \sum_{n \in \text{unocc}} \frac{|\hbar v_{mn}^x|^2 + |\hbar v_{mn}^y|^2 - |-2\Im(\hbar v_{mn}^x \hbar v_{nm}^y)|}{E_{mn}^2} \geq 0. \tag{S26}$$

Note that each term within the summation is positive. Now we multiply both sides by a delta function, $\delta(\hbar\omega + E_{mn})$. This gives us an optical-like trace inequality:

$$\sum_{m \in \text{occ}} \sum_{n \in \text{unocc}} \frac{\Re\sigma_{mn}^{xx}(\mathbf{k}, \omega) + \Re\sigma_{mn}^{yy}(\mathbf{k}, \omega)}{|E_{mn}|} - \Im\bar{\sigma}_{mn}^{xy}(\mathbf{k}, \omega) \geq 0, \tag{S27}$$

where we define $\Re\sigma_{mn}^{aa}(\mathbf{k}, \omega) = c|\hbar v_{mn}^{aa}|^2 \delta(\hbar\omega + E_{mn}) / |E_{mn}|$, and $\Im\bar{\sigma}_{mn}^{xy}(\mathbf{k}, \omega) = c|-2\Im(\hbar v_{mn}^x \hbar v_{nm}^y / E_{mn}^2)| \delta(\hbar\omega + E_{mn})$. The constant, $c = \pi e^2 / \hbar$. Note that the corresponding real or imaginary part of $\sigma_{mn}^{ab}(\mathbf{k}, \omega)$ which are not considered in this study, can also be defined. Here, we introduce the notation for the real part because it is convenient for comparison and allows us to reduce the expression to the original form of optical conductivity easily. From the above equations, we obtain the upper limit on the MBC component at any interband transition contour in the first Brillouin zone:

$$\frac{\Re\sigma_{mn}^{xx}(\mathbf{k}, \omega) + \Re\sigma_{mn}^{yy}(\mathbf{k}, \omega)}{\hbar\omega} \geq \Im\bar{\sigma}_{mn}^{xy}(\mathbf{k}, \omega). \tag{S28}$$

Furthermore, by integrating over the momentum variable, we finally obtain the optical bound on the MBC at each frequency,

$$2 \sum_{m \in occ} \sum_{n \in unocc} \int \frac{d^2 \mathbf{k}}{(2\pi)^2} \frac{\Re \sigma_{mn}^{xx}(\mathbf{k}, \omega) + \Re \sigma_{mn}^{yy}(\mathbf{k}, \omega)}{\hbar \omega} \geq 2 \sum_{m \in occ} \sum_{n \in unocc} \int \frac{d^2 \mathbf{k}}{(2\pi)^2} \Im \bar{\sigma}_{mn}^{xy}(\mathbf{k}, \omega). \quad (\text{S29})$$

Here, we multiply both side of 2 to maintain consistency with the definitions of quantum geometry and topology. Using simpler notation, we can rewrite it as

$$\frac{2[\Re \sigma_{xx}(\omega) + \Re \sigma_{yy}(\omega)]}{\hbar \omega} \geq 2 \Im \bar{\sigma}_{xy}(\omega). \quad (\text{S30})$$

where

$$\Re \sigma_{aa}(\omega) = \sum_{m \in occ} \sum_{n \in unocc} \int \frac{d^2 \mathbf{k}}{(2\pi)^2} \Re \sigma_{mn}^{aa}(\mathbf{k}, \omega), \quad \Im \bar{\sigma}_{xy}(\omega) = \sum_{m \in occ} \sum_{n \in unocc} \int \frac{d^2 \mathbf{k}}{(2\pi)^2} \Im \bar{\sigma}_{mn}^{xy}(\mathbf{k}, \omega). \quad (\text{S31})$$

Importantly, the left-hand term can be obtained through optical response measurements, whereas the right-hand term represents the corresponding imaginary part of the generalized optical Hall conductivity [S36, S58–S60].

4: Souza-Wilkens-Martin sum rule and the relation between optical bound and quantum weight

The SWM sum rule [S53] can be derived directly by integrating the frequency of the real part of the optical conductivity. Let's start with the Kubo-Greenwood formula for optical conductivity:

$$\sigma_{ab}(\omega) = \frac{e^2}{i\hbar} \sum_{m \neq n} \int \frac{d^2 \mathbf{k}}{(2\pi)^2} \frac{f_{mn}(\mathbf{k})}{E_{mn}(\mathbf{k})} \frac{\mathcal{M}_{mn}^a(\mathbf{k}) \mathcal{M}_{nm}^b(\mathbf{k})}{\hbar \omega + E_{mn}(\mathbf{k}) + i0^+}, \quad (\text{S32})$$

where the velocity matrix element is given by $\mathcal{M}_{mn}^a(\mathbf{k}) = \langle u_m(\mathbf{k}) | \hbar \hat{v}_a | u_n(\mathbf{k}) \rangle$, and the velocity operator is $\hat{v}_a = \frac{1}{\hbar} \frac{\partial \hat{H}}{\partial k_a}$. The Fermi-Dirac distribution function is given by $f_n(\mathbf{k}) = 1/[1 + e^{(E_n(\mathbf{k}) - \mu)/k_B T}]$. We denote $f_{mn}(\mathbf{k}) = f_m(\mathbf{k}) - f_n(\mathbf{k})$ and $E_{mn}(\mathbf{k}) = E_m(\mathbf{k}) - E_n(\mathbf{k})$, where $H(\mathbf{k})|u_n(\mathbf{k})\rangle = E_n(\mathbf{k})|u_n(\mathbf{k})\rangle$. The indices a and b represent the directional indices for current and incident electric field, respectively. Here, μ is the chemical potential. The interband contribution to the real part of the optical conductivity in the clean limit can be expressed in terms of the interband Berry connection (see the main context):

$$\Re \sigma_{aa}(\omega) = \pi e^2 \omega \sum_{m \neq n} \int \frac{d^2 \mathbf{k}}{(2\pi)^2} r_{mn}^a r_{nm}^a \delta(\hbar \omega + E_{mn}(\mathbf{k})). \quad (\text{S33})$$

Here, we consider the case of zero temperature. Now, we multiply both sides of Eq. (S33) by a factor of $1/\omega$ and perform a frequency integration. Hence, we have

$$\begin{aligned} \int_0^\infty \frac{\Re \sigma_{aa}(\omega)}{\omega} d\omega &= \pi e^2 \sum_{m \neq n} \int \frac{d^2 \mathbf{k}}{(2\pi)^2} r_{mn}^a r_{nm}^a \int_0^\infty d\omega \delta(\hbar \omega + E_{mn}(\mathbf{k})) \\ &= \frac{\pi e^2}{\hbar} \sum_{m \neq n} \int \frac{d^2 \mathbf{k}}{(2\pi)^2} r_{mn}^a r_{nm}^a \\ &= \frac{\pi e^2}{\hbar} \int \frac{d^2 \mathbf{k}}{(2\pi)^2} g_{aa}(\mathbf{k}), \end{aligned} \quad (\text{S34})$$

which is the SWM sum rule [S53], relating the optical weight to the quantum metric. In the second line, we use the delta function integration formula: $\int_{-\infty}^\infty d\omega f(\omega) \delta(\omega - a) = f(a)$. From the above delta function integration, we can see that all momenta in the Brillouin zone contribute to the integration. Note that negative frequencies have no contribution to the delta function integration.

According to the refined TDI, the integral of the quantum metric relates quantum geometry to topology. To reveal this relationship, we define a quantity called quantum weight [S36], i.e.,

$$\mathcal{K} \equiv 2\pi \int \frac{d^2 \mathbf{k}}{(2\pi)^2} \text{tr}g(\mathbf{k}). \quad (\text{S35})$$

When considering the SWM sum rule for the two directions, we finally obtain

$$\frac{1}{2\pi} \int_0^\infty \frac{2[\Re\sigma_{xx}(\omega) + \Re\sigma_{yy}(\omega)]}{\omega} d\omega = \frac{e^2}{h} \mathcal{K}. \quad (\text{S36})$$

In the practical computation, we replace the ω in the denominator with $\hbar\omega$, i.e.,

$$\frac{1}{2\pi} \int_0^\infty \frac{2\hbar[\Re\sigma_{xx}(\omega) + \Re\sigma_{yy}(\omega)]}{\hbar\omega} d\omega = \frac{e^2}{h} \mathcal{K}. \quad (\text{S37})$$

We calculate $\Re\sigma_{aa}(\omega)$ in units of e^2/h , while the unit of $\hbar\omega$ is eV. In other words, the integral of the optical bound is equal to the quantum weight in units of e^2/h .

5: Upper bound of the quantum weight and the optical gap

Following the steps in Refs. [S36, S53], we will obtain a new upper bound for the optical gap. Due to the semi-positive property of longitudinal optical conductivity, we always have the following inequality:

$$\frac{\hbar}{E_g} \int d\omega \Re\sigma_{aa}(\omega) \geq \int_0^\infty d\omega \frac{\Re\sigma_{aa}(\omega)}{\omega}, \quad (\text{S38})$$

where E_g is the optical gap [S36, S53]. On the other hand, there is the multi-band longitudinal f-sum rule [S80, S124–S126]:

$$\int_0^\infty d\omega \Re\sigma_{aa}(\omega) = \frac{\pi e^2}{2} \sum_{m,n} \int \frac{d\mathbf{k}}{(2\pi)^2} [M_{mn}^{-1}(\mathbf{k})]_{aa} \langle c_{\mathbf{k}m}^\dagger c_{\mathbf{k}n} \rangle, \quad (\text{S39})$$

where the inverse mass tensor is given by $[M_{mn}^{-1}(\mathbf{k})]_{aa} = \sum_{\alpha\beta} U_{m,\alpha}^\dagger(\mathbf{k}) \frac{\partial^2 H_{\alpha\beta}(\mathbf{k})}{\partial(\hbar k_a)^2} U_{\beta,n}(\mathbf{k})$. Here, α and β label the internal degrees of freedom, such as orbital, site, and spin. $H_{\alpha\beta}(\mathbf{k})$ is the matrix element of the non-interacting Hamiltonian. We only consider the non-interacting case, which leads to a greatly simplified form. Combining this with the integrated TDI,

$$\mathcal{K} \geq 2\mathcal{V} \geq \sum_{s=1}^{sec} |\mathcal{N}_s|, \quad (\text{S40})$$

we have derived a longer inequality:

$$\frac{\pi \hbar^2}{E_g} \sum_n \int \frac{d\mathbf{k}}{(2\pi)^2} ([M_{nn}^{-1}(\mathbf{k})]_{xx} + [M_{nn}^{-1}(\mathbf{k})]_{yy}) f_n(\mathbf{k}) \geq \mathcal{K} \geq 2\mathcal{V} \geq \sum_{s=1}^{sec} |\mathcal{N}_s|, \quad (\text{S41})$$

which shows that a larger E_g implies a tighter difference between each quantity if the inverse mass tensor has only slight variations. We can also obtain an upper bound for the optical gap:

$$\frac{\pi \hbar^2}{2\mathcal{V}} \sum_n \int \frac{d\mathbf{k}}{(2\pi)^2} ([M_{nn}^{-1}(\mathbf{k})]_{xx} + [M_{nn}^{-1}(\mathbf{k})]_{yy}) f_n(\mathbf{k}) \geq E_g. \quad (\text{S42})$$

If the non-interacting Hamiltonian is given by $\hbar^2 \mathbf{k}^2 / (2m_e)$ [S36, S49], it can be simplified to:

$$\frac{\pi \hbar^2 n_e}{2m_e \mathcal{V}} \geq E_g, \quad (\text{S43})$$

where n_e is the electron density. In other words, particle density, electron mass, and quantum volume directly constrain the maximum size of the optical gap.

6: Numerical results on band structure and quantum weight during the topological phase transition for the three models

In this section, we provide some numerical results to better understand the physical properties of topological phase transitions for the three models mentioned in the main text. All figures use the same parameters as those in Figs. 1 and 2 (see the main text).

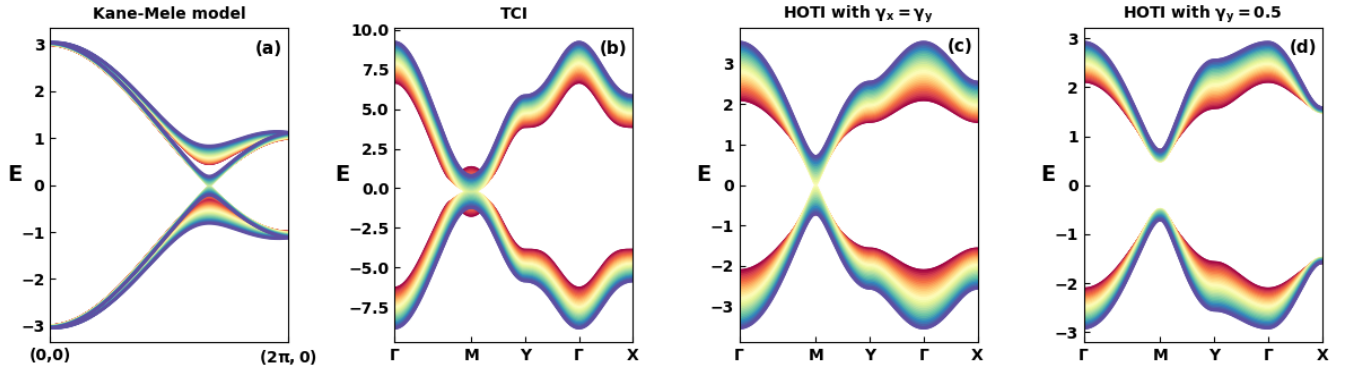


FIG. S1. Band structure of the three models as a function of m along the selected Brillouin zone path near the topological phase transition. (a) $m \in (0, 0.5)$. (b) $m \in (2.5, 5)$. (c,d) $m \in (0.5, 1.5)$.

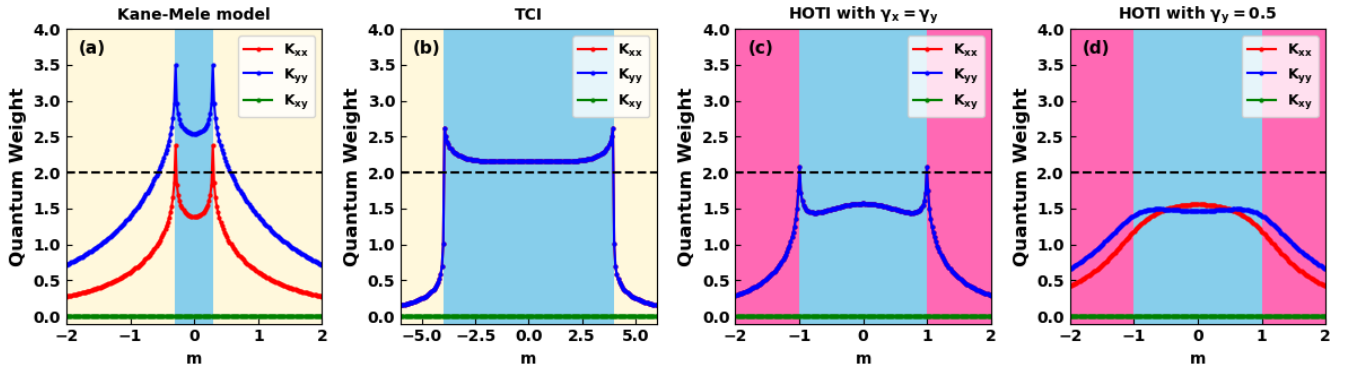


FIG. S2. Optical weight of the three models as a function of m . The figures clearly show the anisotropy (a, d) and isotropy (b, c) of the quantum metric in the x and y directions. In panels (a, b, c), the optical weight exhibits discontinuous behavior at the critical point, while in panel (d), the transition is smooth, corresponding to another type of topological phase transition without gap closing. Here, the optical weight is given by $K_{ab} \equiv 2\pi \int \frac{d^2 k}{(2\pi)^2} g_{ab}(\mathbf{k})$.